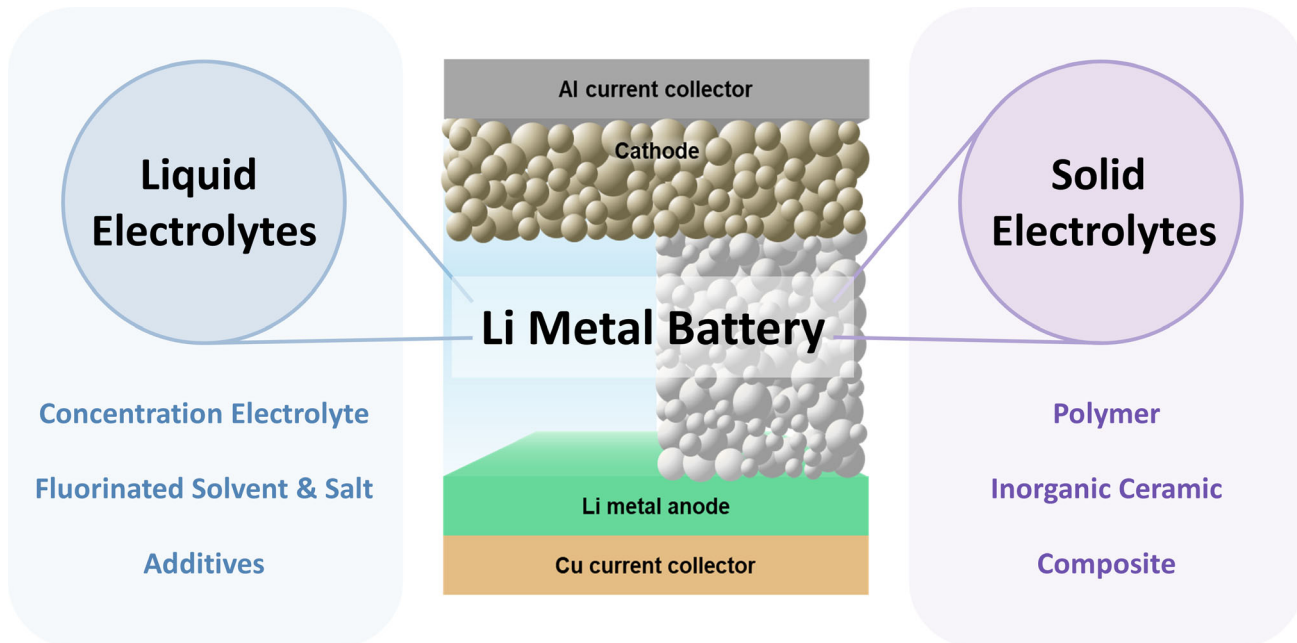


# Design Strategies for Electrolytes in Lithium Metal Batteries: Insights into Liquid and Solid-State Systems

Un Hwan Lee, Seonhye Park, and Joonhee Kang\*



Lithium metal anodes are considered indispensable for next-generation high-energy batteries, but their practical application is severely hampered by interfacial instabilities that lead to uncontrolled dendrite growth and continuous electrolyte consumption. This review systematically addresses these challenges by evaluating state-of-the-art electrolyte engineering strategies for both liquid and solid-state systems. In liquid electrolytes, key approaches are analyzed, including high-concentration/localized formulations, fluorinated components, and functional additives designed to form robust and stable solid electrolyte interphases.

For solid-state electrolytes, advances in polymer, inorganic, and composite systems are surveyed, aimed at enhancing ionic conductivity while mechanically suppressing dendrites. Finally, a forward-looking perspective is proposed, highlighting that the integration of multiscale simulation, machine learning, and data-driven screening will be key to the rational design and rapid discovery of advanced electrolytes. This integrated approach is expected to overcome a critical bottleneck, paving the way for the realization of safe and high-performance lithium metal batteries.

## 1. Introduction

As human civilization progresses and dependence on electricity grows, technologies such as portable electronic devices, electric vehicles, and energy storage systems have become essential. In particular, energy storage has gained increasing importance in light of recent developments in artificial intelligence and computing. Accordingly, the development of rechargeable batteries capable of efficiently storing and delivering electric power has become increasingly critical, among which the lithium-ion batteries (LIBs) have emerged as the most successful and pivotal energy storage technology.<sup>[1–3]</sup> However, conventional LIBs are fundamentally limited by the low theoretical capacity of the graphite anode ( $372 \text{ mAh g}^{-1}$ ) and their reliance on the reversible intercalation/deintercalation of  $\text{Li}^+$  ions, which inherently restricts the maximum achievable energy density.<sup>[1]</sup> In particular, the rapid growth of high-energy-demanding applications such as electric vehicles and aerospace systems has intensified the need for higher energy density, greater power performance, and longer cycle life requirements that current LIB technologies struggle to fully meet.<sup>[4–6]</sup>

To address these limitations, lithium metal is regarded as an irreplaceable anode material, as it possesses the ultrahigh theoretical specific capacity ( $3860 \text{ mAh g}^{-1}$ , or  $2061 \text{ mAh cm}^{-3}$ ), the lowest electrochemical potential ( $-3.04 \text{ V}$  vs. the standard hydrogen electrode), the lowest density ( $0.53 \text{ g cm}^{-3}$ ), and no significant volume expansion during cycle.<sup>[7–9]</sup> These properties

make it particularly suitable for various high-energy applications that demand higher energy density and extended driving range. Notably, next-generation batteries employing Li metal anodes, such as Li-S and Li-air systems exhibit exceptionally high specific energies ( $\approx 650$  and  $\approx 950 \text{ Wh kg}^{-1}$ , respectively).<sup>[7,10]</sup> However, the practical application of Li metal as an anode remains highly challenging and requires precise interfacial control. Because the electrochemical potential of the Li metal anode lies above the lowest unoccupied molecular orbital (LUMO) of most electrolyte systems, spontaneous reduction of the electrolyte occurs, leading to the formation of a solid electrolyte interphase (SEI).<sup>[11]</sup> In conventional LIBs, this SEI plays a critical role by conducting  $\text{Li}^+$  ions while blocking electrons, thereby enabling stable and reversible operation. However, due to the highly negative electrochemical potential of the  $\text{Li}^+/\text{Li}$ , the reduction of the electrolyte occurs more readily and rapidly on Li metal surfaces. During charging,  $\text{Li}^+$  ions are deposited directly onto the Li metal surface, which often leads to the formation of nonuniform and unstable SEI layers.<sup>[12]</sup>

Once such unstable SEI layers are formed on the Li metal surface, they are prone to cracking during cycling, exposing fresh Li metal to the electrolyte and triggering further parasitic reduction reactions. This process promotes the formation of lithium dendrites and electrically isolated dead lithium, which can ultimately lead to severe safety issues such as internal short circuits.<sup>[13–15]</sup> Therefore, addressing these interfacial instabilities is essential for the successful commercialization of lithium metal batteries (LMBs).<sup>[16]</sup> In response, substantial research efforts have been dedicated to designing and developing electrolytes that can stabilize the Li metal-electrolyte interface. These electrolytes are being tailored to achieve several key objectives, including the formation of stable and uniform SEI layers, suppression of lithium dendrite growth, enhancement of  $\text{Li}^+$  ion transport properties, and improvement of both electrochemical and thermal stability. To meet these diverse and demanding requirements, both liquid and solid electrolyte systems are actively being investigated, with each class being developed to fulfill specific design goals.<sup>[17,18]</sup> For example, liquid electrolytes such as conventional organic solvents formulations are designed to form chemically stable SEI layers while simultaneously enabling efficient ion transport at the electrode-electrolyte interface. In contrast, solid-state electrolytes (SSEs) composed of polymer-based or inorganic ceramic

U. H. Lee, S. Park, J. Kang

Department of Nano Fusion Technology

Pusan National University

2 Busandaehak-ro 63-beon-gil, Geumjeong-gu, Busan 46241, Republic of Korea

E-mail: j.kang@pusan.ac.kr

J. Kang

Department of Nanoenergy Engineering

Pusan National University

2 Busandaehak-ro 63-beon-gil, Geumjeong-gu, Busan 46241, Republic of Korea

© 2025 The Author(s). *Batteries & Supercaps* published by Wiley-VCH GmbH. This is an open access article under the terms of the Creative Commons Attribution-NonCommercial-NoDerivs License, which permits use and distribution in any medium, provided the original work is properly cited, the use is non-commercial and no modifications or adaptations are made.

materials are primarily designed to suppress dendrite growth mechanically, reduce flammability risks, and extend battery cycle life by providing robust physical barriers and improved chemical stability.

This review addresses the principal challenges encountered in LMBs and systematically evaluates the strategies developed to overcome them. In particular, focusing on approaches from the perspective of electrolyte design, the discussion is organized into two main sections: liquid electrolytes and SSEs (**Figure 1**). In the liquid electrolyte section, we summarize a range of approaches aimed at mitigating unstable SEI formation, continuous electrolyte decomposition, and dendrite growth in conventional organic-solvent systems. In the solid-state electrolyte section, we survey advances in polymer-based, inorganic-ceramic, and composite electrolyte systems designed to address interfacial instability with Li metal, inherently low ionic conductivity, and mechanical brittleness. Through this discussion, the review aims to provide an integrated overview of electrolyte engineering research in LMBs and to offer insights into future research directions.

## 2. LMBs with Liquid Electrolytes

In conventional LIBs, the standard electrolyte—1 M LiPF<sub>6</sub> in EC-EMC (3:7, v/v)—forms a thin and uniform SEI on the graphite anode, enabling Coulombic efficiencies above 99% and long cycle life.<sup>[2]</sup> However, applying the same electrolyte to Li metal batteries introduces distinct challenges. Because Li metal has a lower electrochemical potential than graphite (LiC<sub>6</sub>) and Li metal surface directly contacts the electrolyte, rapid reductive decomposition of electrolyte occurs.<sup>[7]</sup> The resulting SEI is compositionally heterogeneous and mechanically weak, and the repeated volume changes during cycling create cracks that locally induce Li deposition and promote dendrite growth. These dendrites can penetrate the separator, causing short circuits and risking thermal

runaway. Moreover, the accumulation of dead Li and continuous electrolyte consumption rapidly deplete active material. The electrolyte must also maintain stable compatibility with Al current collectors and high-voltage transition-metal oxide cathodes ( $\geq 4.3$  V). Otherwise, oxidative decomposition of the anion can corrode the Al current collector and leach transition-metal ions from the cathode, preventing stable operation at high voltages. Therefore, the performance and safety of LMBs depend critically on precise control of electrolyte, Li<sup>+</sup> solvation structures, and interfacial reaction pathways. To address these challenges, electrolyte engineering has emerged as a powerful strategy, focusing on molecular-level tuning of solvent-salt interactions and interfacial mechanisms.

In this chapter, we review these electrolyte engineering strategies across three key directions. First, we discuss high-concentration electrolytes (HCEs), which enhance Li<sup>+</sup>-anion interactions to promote inorganic-rich SEI formation, and localized HCEs (LHCEs), which mitigate HCE viscosity and conductivity issues via inert or functional diluents. Second, we examine fluorinated solvents and salts, where fluorine incorporation improves both reductive and oxidative stability, inhibits Al corrosion, and yields robust cathode interphases. Finally, we cover additive-based approaches, in which small amounts of functional additives selectively decompose to tailor interfacial reactions and precisely engineer SEI/Cathode-electrolyte interphase (CEI) architectures.

### 2.1. Concentration Electrolytes

In LMBs, the high reactivity of Li metal anode inevitably drives electrolyte decomposition, so SEI is formed on the anode. Notably, SEI dominated by inorganic species (e.g., LiF, Li<sub>2</sub>O, Li<sub>3</sub>N), rather than organic species, delivers superior mechanical robustness and chemical stability.<sup>[19,20]</sup> Accordingly, HCEs have emerged as an effective way to bias the initial reduction toward the salt anion (**Figure 2a**). When the salt concentration rises above 4 M, anions are increasingly incorporated into the primary



**Un Hwan Lee** is currently pursuing his master's degree in the Department of Nano Fusion Technology at Pusan National University, Republic of Korea, under the supervision of Prof. Joonhee Kang. He received his B.S. in energy engineering from Pusan National University in 2025. His research interests focus on computational chemistry and battery materials, particularly the development of lithium metal batteries, electrolyte engineering, and machine-learning interatomic potentials.



**Seonhye Park** is a master's student in the Department of Nano Fusion Technology at Pusan National University, under the supervision of Prof. Joonhee Kang. She received her B.S. in chemical engineering from the University of Ulsan in 2024. Her current research focuses on solid-state electrolytes for lithium metal batteries, with an emphasis on property prediction and material design using density functional theory and machine-learning interatomic potentials.



**Joonhee Kang** is an associate professor in the Department of Nano Fusion Technology at Pusan National University (PNU), Republic of Korea. He holds a B.S. in physics from the University of Seoul and earned his Ph.D. in Energy Systems Engineering from the Daegu Gyeongbuk Institute of Science and Technology (DGIST). Prior to his appointment at PNU, he served as a senior researcher at the Korea Institute of Energy Research. His research interests encompass computational materials science, energy storage systems, and data-driven materials design. He specializes in lithium metal batteries, solid-state electrolytes, and the structural stability of electrode-electrolyte interfaces. Utilizing density functional theory and machine-learning interatomic potentials, his work aims to advance the understanding and development of next-generation energy storage technologies.

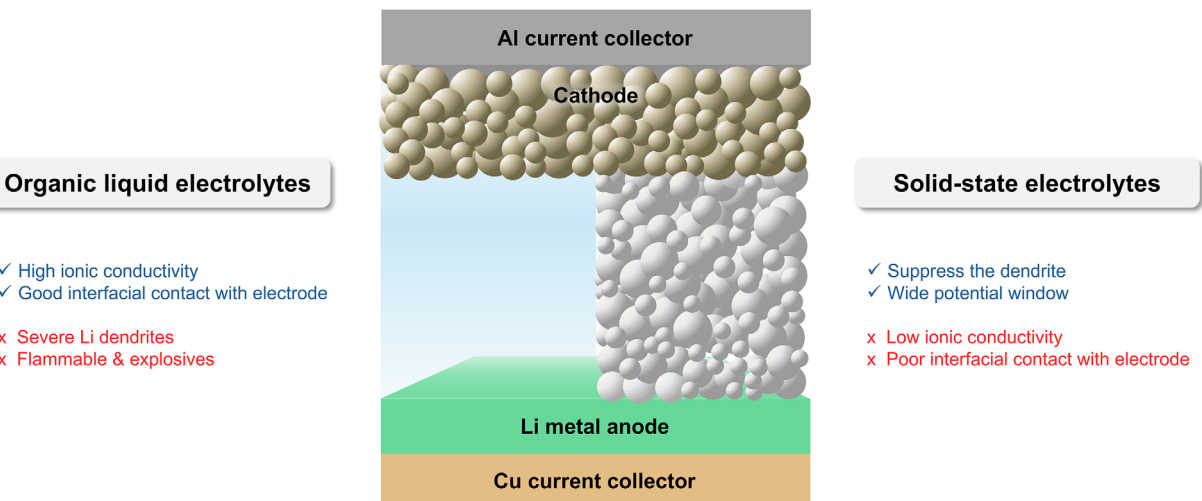


Figure 1. Schematic illustration of LMBs employing (left) organic liquid electrolyte and (right) SSE.

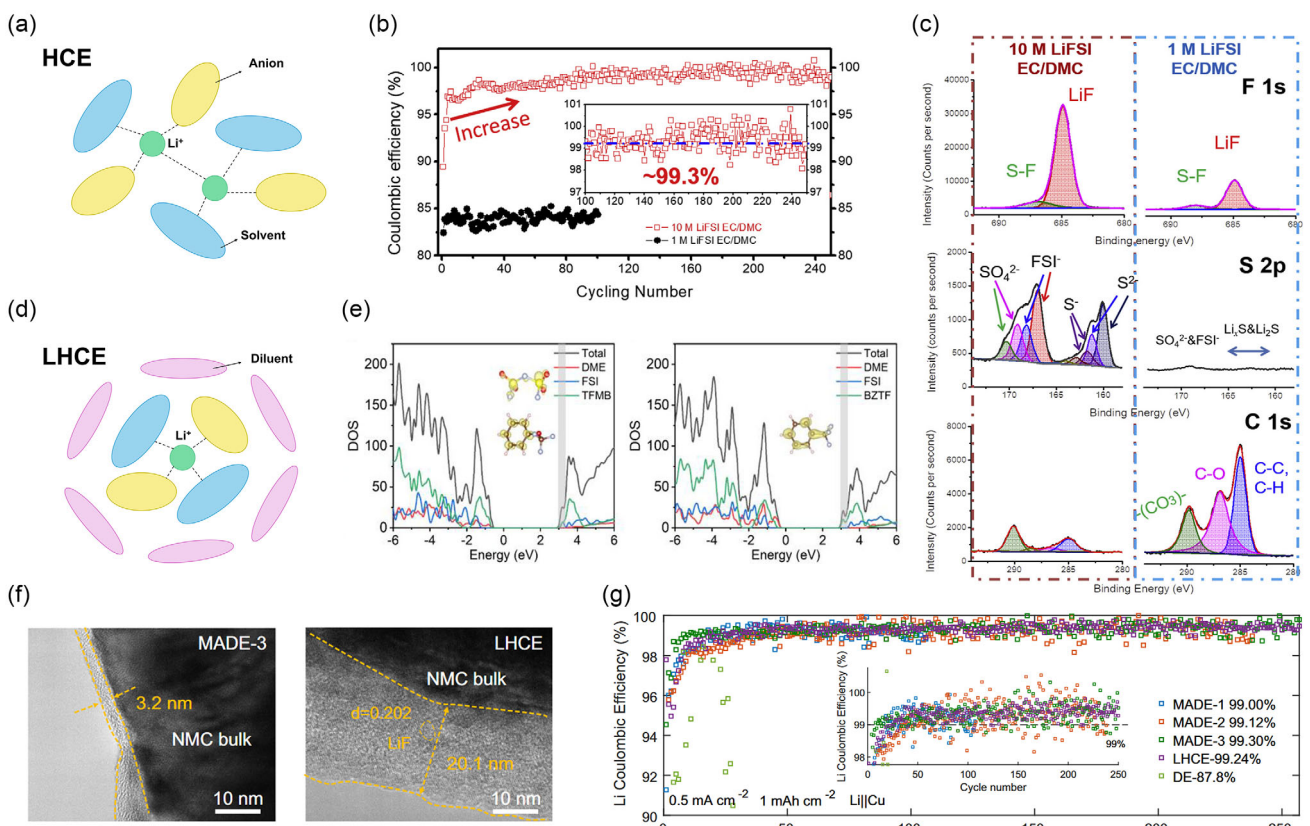


Figure 2. a) Schematic illustration of the solvation environment in an HCE. b) Coulombic efficiency at  $0.2 \text{ mA cm}^{-2}$  for 1 and 10 M LiFSI-EC/DMC. c) XPS analysis of the SEI formed on the Li metal anode cycled in concentrated EC/DMC and diluted EC/DMC electrolyte. Reproduced with permission.<sup>[22]</sup> Copyright 2017, Elsevier. d) Schematic illustration of the solvation environment in an LHCE. e) DOS obtained in DFT-AIMD simulations for LHCE-TFMB and LHCE-BZTF. Reproduced with permission.<sup>[26]</sup> Copyright 2022, American Chemical Society. f) High-resolution TEM images of the cathodes after 50 cycles in MACE-3 and LHCE. g) Coulombic efficiency in Li|Cu cells at  $0.5 \text{ mA cm}^{-2}$  and  $1 \text{ mAh cm}^{-2}$  (Insert: enlarged view of Li CE). Reproduced with permission.<sup>[27]</sup> Copyright 2024, Springer Nature.

$\text{Li}^+$  solvation shell. As a result, compared with a low-concentration electrolytes, the fraction of solvent-separated ion pairs decreases, while contact ion pairs (CIPs) and aggregates (AGGs) become the

predominant species, fundamentally restructuring the solvation environment. Because most solvent molecules participate in coordinating both  $\text{Li}^+$  and anion, the concentration of free

solvent is markedly reduced. This anion-rich, solvent-poor solvation environment shifts the initial reduction preferentially toward the anion, driving the formation of an inorganic-rich SEI that significantly enhances the stability of the Li metal anode. Qian et al. employed the ether solvent 1,2-dimethoxyethane (DME) in combination with a 4 M LiFSI electrolyte to realize stable Li plating and stripping at high current densities.<sup>[17]</sup> Because DME has a low reduction potential (1.68 V vs. Li/Li<sup>+</sup>), it is less prone to direct reaction with Li metal, and at 4 M the prevalence of CIPs and AGGs further suppresses parasitic reactions. Consequently, a Coulombic efficiency of 98.4% was maintained at 4 mA cm<sup>-2</sup>, far exceeding that obtained with a conventional 1 M electrolyte. Nevertheless, the oxidative stability of ether solvents is limited to <4 V, restricting their use with high-voltage cathodes such as Ni-rich NMC. By contrast, carbonate solvents exhibit higher oxidative stability (>4.3 V) and are therefore widely adopted in commercial high-voltage LIBs.<sup>[21]</sup> Fan et al. incorporated LiFSI into carbonate solvents at concentrations up to 10 M, realizing an electrolyte that stabilizes both the Li metal anode and high-voltage cathodes.<sup>[22]</sup> The 10 M LiFSI EC/DMC electrolyte achieves a coulombic efficiency (CE) of 99.6% at 4.6 V and retains 86% capacity after 100 cycles (Figure 2b). This performance stems from the formation of a LiF-rich, organic-poor SEI on the Li metal surface and F-rich CEI on NMC622 (Figure 2c). Suo et al. developed a full-fluoride electrolyte by dissolving LiFSI in FEC solvent at 7 M, thereby establishing stable interphases on both the Li metal anode and high-voltage cathode.<sup>[23]</sup> This 7 M LiFSI-FEC electrolyte maintains oxidative stability above 5 V and, through the formation of LiF-rich SEI and CEI, achieves a CE of 99.6% and 78% capacity retention after 130 cycles, enabling 5 V-class LMBs.

However, despite their exceptional performance, HCEs suffer from high viscosity, low ionic conductivity, poor wettability, and elevated cost, which hinder their industrial deployment. Accordingly, the LHCEs have been introduced, in which inert diluents are added to HCEs to reduce viscosity and enhance ionic conductivity (Figure 2d). For example, fluorinated ethers such as bis(2,2,2-trifluoroethyl) ether (BTFE) and 1,1,2,2-tetrafluoroethyl 2,2,3,3-tetrafluoropropyl ether (TTE) are introduced as diluents in HCEs and do not participate in the primary Li<sup>+</sup> solvation shell. This preserves the original solvation structure while reducing viscosity and improving ionic conductivity. Through this LHCEs approach, the addition of BTFE to a 5.5 M LiFSI-DMC electrolyte raises the CE to 99.5%, and a LiFSI-DME LHCE diluted with TTE at a 3:1 molar ratio attains over 99.3% CE and stable cycling beyond 155 cycles at 4.5 V.<sup>[24,25]</sup> However, conventional diluents such as TTE possess excessively high reductive stability and thus fail to contribute to SEI formation, acting solely as viscosity modifiers. To overcome this limitation, recent efforts have focused on designing diluents with tailored structural and electronic properties capable of directly participating in SEI formation. Zhu et al. introduced fluorinated aromatic diluents—trifluoromethoxybenzene (TFMB) and benzotrifluoride (BZTF)—into a 1.8–2.0 M LiFSI-DME electrolyte to create a novel LHCE.<sup>[26]</sup> Although these diluents do not engage the primary Li<sup>+</sup> solvation shell, density of states (DOS) analysis via density functional theory (DFT) reveals that the LUMO is delocalized over TFMB and FSI<sup>-</sup>, whereas in the BZTF system it lies

predominantly on the BZTF molecule (Figure 2e). This distribution implies that TFMB and FSI<sup>-</sup> undergo coreduction, while BZTF preferentially decomposes, in both cases promoting LiF-rich SEI formation. Such band-structure analysis highlights the direct role of diluents in interfacial chemistry, beyond their conventional role as mere viscosity modifiers. Consequently, the TFMB/BZTF-containing LHCE yields a thinner and more compact SEI and CEI than conventional TTE-based systems, delivering >99.7% CE and 80% capacity retention over 260 cycles. In conventional LHCEs, Cui et al. identified that exothermic Li salt-electrode reactions at both the anode and cathode still pose a significant thermal runaway hazard.<sup>[27]</sup> To overcome this, they introduced the molecular anchoring diluent electrolyte (MADE) concept, in which strong and nonconventional hydrogen bonds form between the fluorinated ether diluent (TTE) and DME, effectively constraining the reactivity of free solvent molecules. This electrolyte extends the oxidative stability beyond 4.7 V and raises the thermal runaway onset temperature from 141 to 209 °C. MADE electrolytes form ultrathin cathode-electrolyte interphases (1–3.2 nm) compared with 20.1 nm for a TTE-based LHCE (Figure 2f), and in Li|NMC811 cells achieve average CE of 99.3% (MADE-3) (Figure 2g). More recently, Liu et al. reported an acetonitrile-based LHCE (LiFSI-AN diluted with TTE) that enabled stable cycling of Ni-rich NMC811 cathodes at subzero temperatures, retaining 113 mAh g<sup>-1</sup> at -40 °C and 85.5% capacity after 90 cycles at -30 °C.<sup>[28]</sup> Electrochemical impedance spectroscopy confirmed suppressed charge-transfer resistance, while CEI stabilization was achieved via anion-derived decomposition. This work illustrates the potential of LHCEs in expanding the operational temperature window of LMBs, although the presence of free AN still imposes challenges for SEI stability on Li metal anodes. Meanwhile, Efaw et al. proposed that LHCEs exhibit a micelle-like microstructure, in which salt-solvent clusters are stabilized by surfactant-like solvent shells and embedded within a diluent matrix.<sup>[29]</sup> Through molecular dynamics (MD) simulations, Raman spectroscopy, and small-angle and wide-angle X-ray scattering, they revealed that this structuring increases local salt concentration, enhances Li<sup>+</sup>-FSI<sup>-</sup> association, and facilitates the formation of uniform, inorganic-rich SEI. A peak in the AGG<sup>+/</sup>/AGG ratio at 25 °C correlated with the most stable SEI and best cycling performance.

## 2.2. Fluorinated Solvent and Salt

Recent developments in HCEs and LHCEs have enabled the transformation of Li<sup>+</sup> solvation structures into anion-rich configurations, thereby promoting the formation of inorganic-rich SEI and CEI that significantly enhance the cycle life of LMBs. Nevertheless, carbonate-based solvents, despite their high oxidative stability, suffer from poor compatibility with Li metal due to excessive reduction decomposition. In contrast, ether-based solvents exhibit strong interface compatibility with Li metal but are intrinsically limited by low oxidative stability, rendering them incompatible with high-voltage cathodes (>4.5). A promising strategy to simultaneously address these challenges is the selective fluorination of solvent molecules, which aims to regulate their redox properties and interfacial reactivity. The strong

electron-withdrawing nature of  $-CF_x$  groups lowers both the LUMO and the highest occupied molecular orbital (HOMO) energy levels of the solvent molecules. This modulation enhances reductive and oxidative stability simultaneously. The lowered LUMO facilitates rapid reduction on the Li metal surface, promoting the formation of an inorganic SEI, and the lowered HOMO extends the oxidation resistance of the solvent, enabling stable operation at voltages up to 5–6 V.<sup>[30]</sup>

Importantly, fluorine introduced through  $-CF_3$  substitution predominantly exists as LiF in the SEI, which serves as the main inorganic component imparting mechanical robustness and ionic conductivity. LiF is primarily formed via the reductive decomposition of fluorinated solvents or imide-based salts at the Li metal interface. This mechanism has been consistently verified by X-ray photoelectron spectroscopy (XPS), showing the characteristic F 1s peak of LiF at  $\approx$ 685 eV, and by transmission electron microscopy (TEM), which reveals thin and compact SEI layers with uniform thickness distribution. Together, these results confirm that the LiF-rich SEI is the critical factor stabilizing Li deposition and suppressing dendritic growth in fluorinated electrolyte systems. This dual interfacial stabilization mechanism provides a promising design framework for constructing electrolytes compatible with both Li metal anode and high-voltage cathode. In this section, we

discuss the design principles and electrochemical performance of fluorinated systems.

Yu et al. designed a fluorinated ether solvent, 1,4-dimethoxybutane (FDMB), by extending the ethane backbone of DME to butane and substituting the two central carbon atoms with  $-CF_2$ -groups (Figure 3a).<sup>[31]</sup> In this molecular structure, Li<sup>+</sup> ions are simultaneously coordinated by both oxygen and fluorine atoms, leading to weak Li<sup>+</sup>-solvent interactions. Consequently, the FSI<sup>-</sup>/solvent ratio in the primary Li<sup>+</sup> solvation shell increases to 3.29:1, establishing a highly anion-rich solvation environment (Figure 3b). This modified solvation structure facilitates the rapid formation of a thin ( $\approx$ 6 nm) LiF-rich SEI layer (Figure 3c), and suppresses corrosion of the Al current collector, thereby extending the oxidative stability beyond 6 V. As a result, Li|NMC cells exhibit an average CE of 99.98% and retain 90% of their capacity after 420 cycles. Building upon this strategy, Wang et al. synthesized a further fluorinated ether solvent, 1,6-dimethoxyhexane (FDMH), by extending the  $-CF_2$ - backbone of FDMB into a six-carbon chain.<sup>[32]</sup> A dual-solvent electrolyte was formulated by combining FDMH and DME (v:v = 6:1) with 1 M LiFSI. In this system, FDMH, DME, and FSI<sup>-</sup> collectively coordinate with Li<sup>+</sup> to form an anion-derived solvation shell, which promotes the formation of an inorganic-rich SEI composed primarily of LiF and Li<sub>2</sub>S. This electrolyte

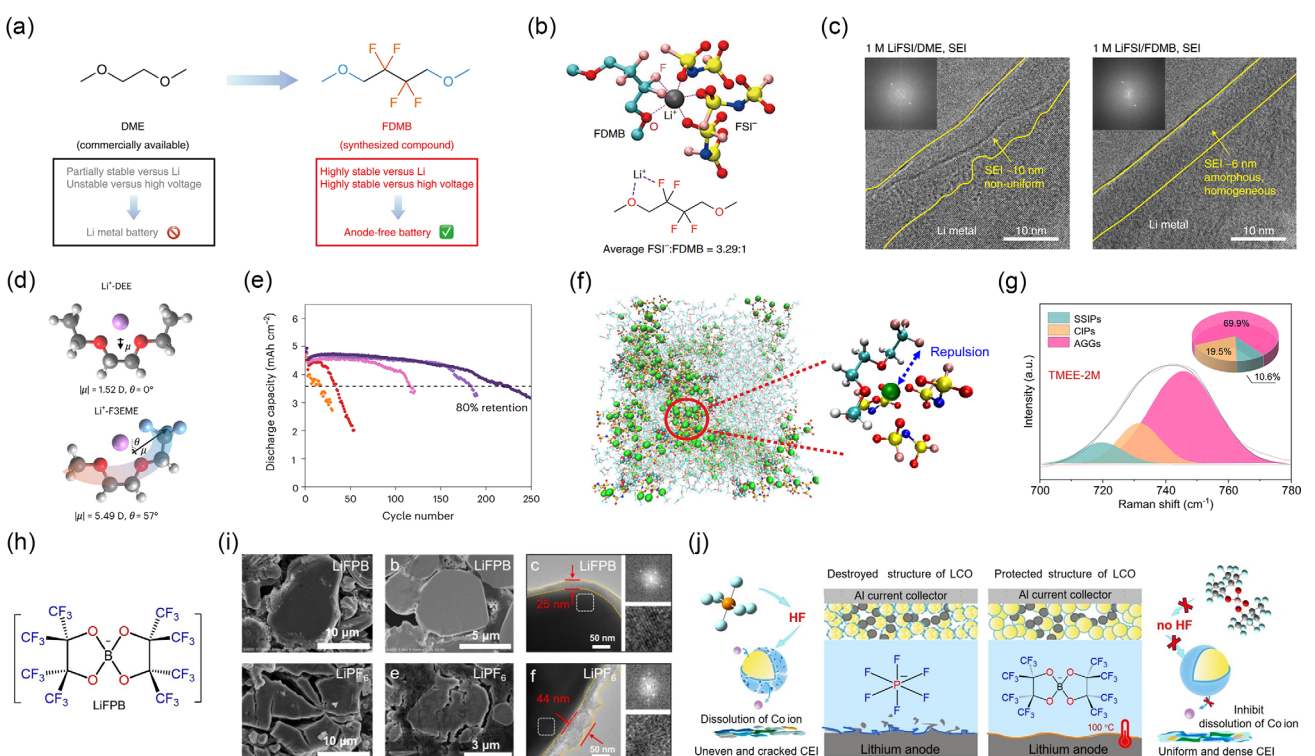


**Figure 3.** a) Molecular design and structures of DME and FDMB and b) solvation structure of 1 M LiFSI/FDMB given by MD simulations and the corresponding average ratio of solvation bindings from FSI<sup>-</sup> anions to those from solvents in the primary solvation shell. c) Cryo-TEM images of the SEI formed in 1 M LiFSI/DME and 1 M LiFSI/FDMB electrolytes. Reproduced with permission.<sup>[31]</sup> Copyright 2020, Springer Nature. d) DFT calculations of ion-induced dipole moment ( $\mu$ ) for Li<sup>+</sup>-coordinated ether solvents, including DEE and F3EME. e) Extended cycling performance of Li|NMC811 under conditions of 50  $\mu$ m Li, 4.9 mAh cm<sup>-2</sup> NMC811, 2.8–4.4 V, 0.5C charge/1C discharge, and E/C = 8 g Ah<sup>-1</sup>. Reproduced with permission.<sup>[33]</sup> Copyright 2025, Springer Nature. f) MD simulation trajectory snapshot of TMEE-2 M electrolyte and extracted solvation structures. (H: white, Li: lime, C: cyan, N: blue, O: red, F: pink, and S: yellow). g) The Raman spectrum of the TMEE-2 M electrolyte. Reproduced with permission.<sup>[34]</sup> Copyright 2025, Springer Nature. h) Design scheme of LiFPB salt molecule. i) SEM, cross-section SEM, and TEM images of LCO cathodes cycled in LiFPB-EC/DMC and LiPF<sub>6</sub>-EC/DMC at 60 °C. j) Schematic illustration of the positive role of LiFPB salt in protecting LCO cathode and Li metal anode. Reproduced with permission.<sup>[35]</sup> Copyright 2024, Wiley-VCH.

demonstrated excellent oxidative stability above 6 V and achieved an average CE of 99.5%. Notably, 20  $\mu\text{m}$  Li|NMC532 full-cells retained 84% of their initial capacity after 250 cycles, and anode-free Cu|NMC811 pouch cells maintained 75% capacity retention after 120 cycles under high-rate, high-voltage conditions. Despite these promising results, the symmetric solvent molecular structure fully encapsulates  $\text{Li}^+$  ions, resulting in solvent-shielding effects that hinder redox kinetics. This leads to a significantly reduced exchange current density, ultimately causing a sharp drop in CE under high-rate operation. To address this limitations of symmetric solvent structures, Choi et al. designed an asymmetric fluorinated ether solvent, 1-(2,2,2-trifluoro)-ethoxy2-methoxyethane (F3EME), by introducing a  $-\text{CF}_3$  group at the  $\beta$ -carbon position.<sup>[33]</sup> This asymmetric geometry enables rapid reorientation of the solvent- $\text{Li}^+$  dipole moment under electric field, thereby minimizing solvent-shielding effects (Figure 3d). As a result, the exchange current density ( $j_0$ ) is significantly improved, facilitating fast redox kinetics and uniform Li deposition. In addition, the electron-withdrawing  $-\text{CF}_3$  group enhances oxidative stability, enabling operation up to 4.6 V. Therefore, Li|NMC811 coin cells demonstrated stable cycling over 220 cycles under 2 mA cm<sup>-2</sup> charge and 4 mA cm<sup>-2</sup> discharge conditions (Figure 3e). Furthermore, anode-free Cu|Ni95 pouch cells maintained over 90% of their capacity over 600 cycles. Additionally, Zhang et al. synthesized a fluorinated ether solvent, 1,1,1-trifluoro-2-(2-methoxyethoxy)ethane (TMEE), by selectively introducing a  $-\text{CF}_3$  group at one terminal of the DME molecule through a monosubstitution strategy.<sup>[34]</sup> Using this solvent, they formulated a 2 M LiFSI TMEE electrolyte. The introduction of a  $-\text{CF}_3$  group in TMEE imparts strong electron-withdrawing and lithiophobic characteristics (Figure 3f), which collectively weaken  $\text{Li}^+$ -solvent coordination and promote the formation of an anion-rich solvation shell (AGGs, 69.9%) (Figure 3g). This solvation environment facilitates the rapid formation of a thin ( $\approx 15$  nm) bilayer SEI and a stable CEI, significantly reducing interfacial resistance. Moreover, the TMEE-based electrolyte achieves a high ionic conductivity of 3.5 mS cm<sup>-1</sup> and a transference number ( $t^+$ ) of 0.81, indicating efficient  $\text{Li}^+$  transport. As a result, Li|NMC811 coin cells (50  $\mu\text{m}$ , 3.5 mAh cm<sup>-2</sup>) retain 88% of their capacity after 450 cycles at 1 C. In addition, a 14 Ah anode-free Cu|NMC811 pouch cell delivers an initial energy density of 512 Wh kg<sup>-1</sup> and retains 90% capacity after 100 cycles. These results demonstrate that TMEE offers a next-generation electrolyte design strategy based on asymmetric  $-\text{CF}_3$  substitution, overcoming the conductivity drawbacks often associated with fluorination while enabling compatibility with high-voltage, high-rate LMBs.

Despite the interfacial stabilization enabled by fluorinated solvents, they do not fully suppress salt decomposition and hydrofluoric acid (HF) generation under high-voltage and high-temperature conditions. To address this limitation, recent studies have focused on the design of lithium salt as critical component of the electrolyte. LiPF<sub>6</sub>, the most commonly used salt in commercial LIBs, exhibits high sensitivity to heat and moisture and shows limited compatibility with Li metal anode and high-voltage cathodes, thereby restricting its use in LMBs.<sup>[35,36]</sup> In contrast, imide-based salts such as LiFSI and LiTFSI provide superior thermal and

chemical stability, but the FSI<sup>-</sup> and TFSI<sup>-</sup> anions severely corrode Al current collectors above 4.3 V. Preventing this corrosion requires high-concentration electrolyte ( $\geq 4$  M), which impose trade-offs such as increased viscosity, reduced ionic diffusivity, and higher cost.<sup>[37]</sup> To overcome the limitations of these conventional salts, recent studies have focused on the development of new fluorinated Li salts. Chen et al. designed lithium perfluoropinacolatoborate (LiFPB) by combining covalent C—F bonds with a borate-based B—O framework, aiming to suppress HF generation and improve thermal stability associated with the ionic P—F bonding in LiPF<sub>6</sub> (Figure 3h).<sup>[38]</sup> The bulky FPB<sup>-</sup> anion exhibits strong electron-withdrawing and leverages the B—O coordination to significantly reduce the  $\text{Li}^+$ -solvent, thereby constructing an anion-rich solvation structure. In 1 M LiFPB EC/DMC electrolyte, an inorganic-rich CEI ( $\approx 25$  nm) and a LiB<sub>x</sub>O<sub>y</sub>/LiF-based SEI are simultaneously formed, effectively minimizing interfacial resistance (Figure 3i). As a result, Li|LCO coin cells (4.45 V, 60 °C) maintained 80% capacity after 260 cycles, and 86% even at 100 °C after 100 cycles. Moreover, stable operation up to 5.2 V was achieved without Al current collector corrosion, demonstrating the potential of LiFPB as a high-voltage, high-temperature compatible salt for LMBs (Figure 3j). In ether-based electrolyte such as DME, the solvent exhibits poor oxidative stability under high-voltage conditions, thus requiring the incorporation of antioxidative Li salts. He et al. developed lithium perfluoro-butanesulfonate (LiPFBS), which extended the oxidation stability limit of DME electrolyte to 4.6 V at a high concentration of 3 M.<sup>[39]</sup> As a result, Li|LCO full cells retained 73% of their capacity after 200 cycles. This improved performance is attributed to the strong coordination between PFBS<sup>-</sup> and  $\text{Li}^+$  at high concentrations, which lowers the LUMO energy and enables the preferential reduction of PFBS<sup>-</sup> to form a LiF-rich inorganic SEI and CEI. Together, FPB<sup>-</sup> (carbonate) and PFBS<sup>-</sup> (ether) represent two distinct fluorinated Li salt design strategies that overcome the limitations of conventional LiPF<sub>6</sub> and LiFSI/TFSI in different solvent environments.

### 2.3. Additives

The concentrated and fluorinated electrolyte examined above fundamentally altered  $\text{Li}^+$  solvation environment, which in turn enhances Li metal stability and expands feasibility of high-voltage battery operation. In contrast, the incorporation of small amounts of redox-active additives has been explored as an effective strategy to regulate SEI/CEI formation through selective interfacial reactions. Among various additives used in organic electrolytes, lithium nitrate (LiNO<sub>3</sub>) has demonstrated effective performance in ether-based systems. However, its application in carbonate-based electrolytes has been severely limited due to its extremely low solubility.

To address these solubility problems, Liu et al. developed a solubility-mediated sustained-release film (LNO-SRF) by dispersing LiNO<sub>3</sub> nanoparticles within PVDF-HFP porous gel matrix (Figure 4a).<sup>[40]</sup> This design enables the continuous release of NO<sub>3</sub><sup>-</sup> during cycling, maintaining a stable local concentration near the electrode surface. The porous structure enabled

homogeneous dispersion of  $\text{LiNO}_3$  without observable agglomeration, as confirmed by scanning electron microscopy (SEM) and uniform nitrogen distribution in energy-dispersive X-ray (EDX) elemental mapping (Figure 4b). The released  $\text{NO}_3^-$  undergoes preferential reduction over other electrolyte components, leading to the formation of a bilayer SEI. Specifically, the SEI consists of a crystalline  $\text{Li}_2\text{O}$  outer layer and an amorphous inner matrix containing  $\text{Li}_2\text{CO}_3$  nanocrystals, as explicitly illustrated and labeled in Figure 4c. This bilayer structure facilitates the formation of spherical Li nuclei and ensures a uniform  $\text{Li}^+$  flux, effectively suppressing dendrite growth. Nevertheless, the LNO-SRF strategy remains insufficient in providing adequate oxidative stability at the high-voltage cathode. To overcome this limitation, Li et al. formulated a dual-additive electrolyte by incorporating 3 wt%  $\text{LiNO}_3$  and 1 wt% tris(pentafluorophenyl)borane (TPFPB) into a 1 M  $\text{LiPF}_6$ -FEC/EMC (3:7, v/v).<sup>[41]</sup> The electron-deficient center of TPFPB facilitates the dissociation of  $\text{LiNO}_3$  clusters, enhancing the solubility of  $\text{LiNO}_3$  in carbonate-based electrolytes. During cycling,  $\text{NO}_3^-$

undergoes preferential reduction at the Li metal anode to form a  $\text{Li}_2\text{O}$ -rich SEI, while TPFPB decomposes at  $\approx 4.3$  V to generate an amorphous CEI containing F/B species on the cathode. This dual-interfacial protection mechanism enables highly stable operation, as evidenced by CE of 98.5% over 300 cycles in  $\text{Cu}|\text{Li}$  cells. Furthermore, a NCM811 full cell ( $3.4 \text{ mAh cm}^{-2}$ ) delivered an initial energy density of  $\approx 295 \text{ Wh kg}^{-1}$  and retained 80% of its capacity after 140 cycles. Furthermore, to address the critical challenges of ion transport and dendrite growth under ultralow temperature ( $< -60^\circ\text{C}$ ), Zhang et al. developed a multifunctional additive, perfluoroalkylsulfonyl quaternary ammonium nitrate (PQA- $\text{NO}_3^-$ ), by coupling nitrate ( $\text{NO}_3^-$ ) with a quaternary ammonium cation (PQA $^+$ ).<sup>[42]</sup> The PQA $^+$  that has low LUMO energy undergoes preferential reduction on the Li metal anode, rapidly forming an inorganic-rich SEI composed of  $\text{LiF}$ ,  $\text{Li}_3\text{N}$ ,  $\text{Li}_2\text{O}$ , and  $\text{Li}_2\text{S}$  (Figure 4d). This passivation layer effectively suppress electron tunneling and provide fast  $\text{Li}^+$  conduction channels. Simultaneously,  $\text{NO}_3^-$  enters the  $\text{Li}^+$  solvation shell via

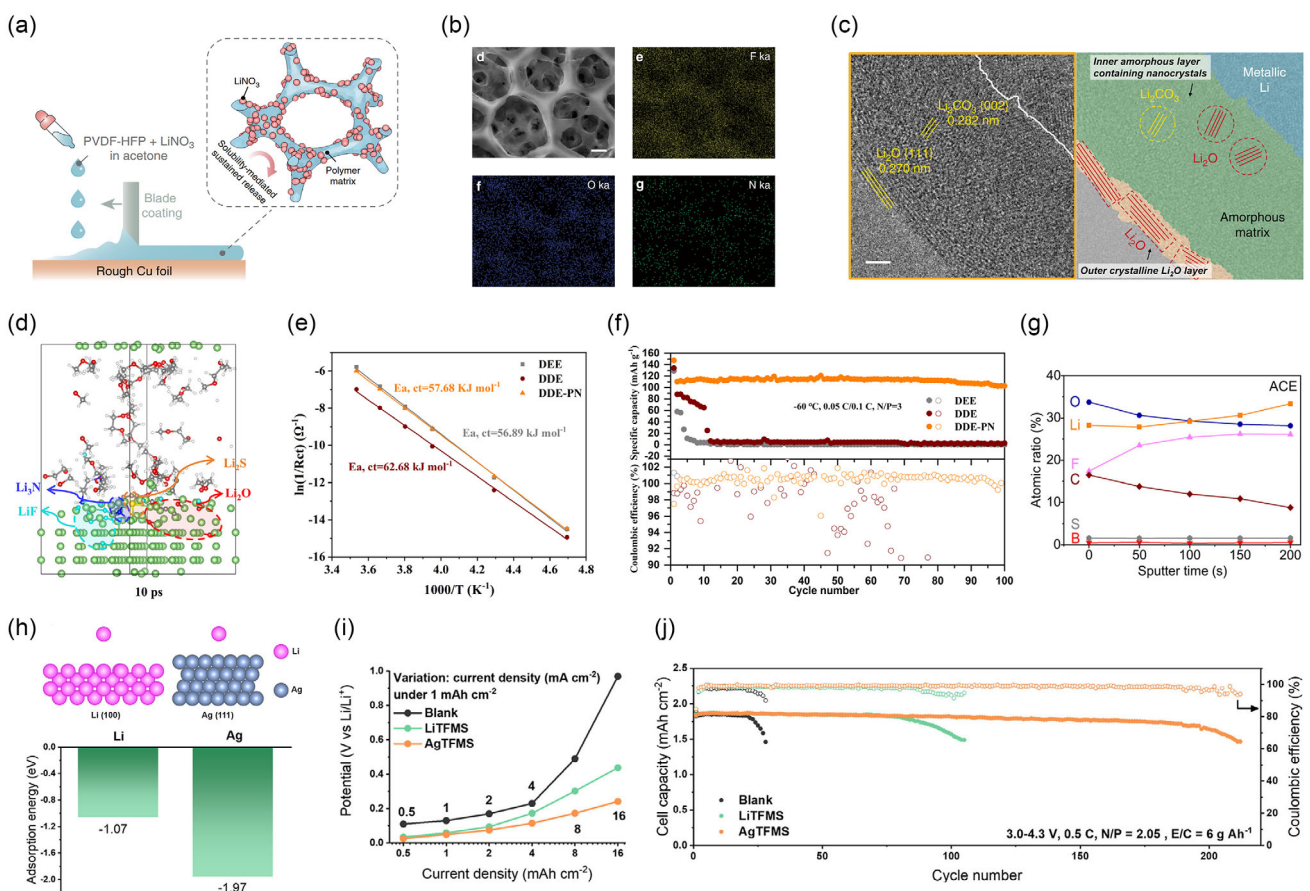


**Figure 4.** a) Schematic illustration the LNO-SRF architecture and its working principle. b) High-magnification SEM image and the corresponding EDX elemental mappings of LNO-SRF (Scale bar,  $2 \mu\text{m}$ ). c) Detailed TEM image and the corresponding schematic of the bilayer SEI. The outside is a dense layer of  $\text{Li}_2\text{O}$  and the inside is an amorphous matrix with crystalline domains ( $\text{Li}_2\text{O}$  and  $\text{Li}_2\text{CO}_3$ ). Reproduced with permission.<sup>[40]</sup> Copyright 2018, Springer Nature. d) AIMD simulation snapshot of decomposition reaction processes between PN with Li metal. (F: cyan, C: gray, N: blue, O: red, S: yellow, H: white, and Li: green). e) The activation energies for  $\text{Li}^+$  desolvation at the negative electrode interface. f) Cycling performance of full cells at  $-60^\circ\text{C}$ . Reproduced with permission.<sup>[42]</sup> Copyright 2025, Springer Nature. g) XPS characterization of cycled Li metal anode. Atomic composition ratios at different sputtering times using ACE. Reproduced with permission.<sup>[43]</sup> Copyright 2024, The Royal Society of Chemistry. h) Illustration of Li adsorption on  $\text{Li}(100)$  and  $\text{Ag}(111)$  surfaces alongside computed adsorption energy. i) Overpotential profiles during Li stripping reaction of  $\text{Li}|\text{Li}$  cells at  $1 \text{ mAh cm}^{-2}$ . j) Cycle performance profiles of  $\text{Li}|\text{NMC811}$  cells ( $\text{N/P} = 2.05$ ,  $\text{E/C} = 6 \text{ g Ah}^{-1}$ ). Reproduced with permission.<sup>[45]</sup> Copyright 2025, Wiley-VCH.

competitive coordination, establishing a solvent-poor, anion-rich coordination environment and reducing the desolvation energy barrier to  $56.89 \text{ kJ mol}^{-1}$  (Figure 4e). In addition, the  $\text{NO}_3^-$ -dominated electric double layer extends the anodic stability of ether-based electrolytes to 4.3 V, enabling both high-rate Li|NMC 811 cycling and dendrite-free Li deposition even below  $-60^\circ\text{C}$  (Figure 4f).

Beyond conventional  $\text{LiNO}_3$ -based additives, recent studies have actively explored the incorporation of functional additives to further reinforce the electrode electrolyte interface. Ryu et al. introduced a functional additive, tetrabutylammonium tetrafluoroborate (TBATFB), composed of a bulky tetrabutylammonium ( $\text{TBA}^+$ ) cation and a tetrafluoroborate ( $\text{TFB}^-$ ) anion.<sup>[43]</sup> The  $\text{TBA}^+$  cation forms a self-assembled barrier layer on the Li metal surface, which spatially regulates  $\text{Li}^+$  flux and promotes uniform nucleation and compact deposition, effectively suppressing dendrite growth. In parallel, the  $\text{TFB}^-$  anion undergoes interfacial reactions with the Li metal surface, inducing rapid formation of a LiF-rich SEI through efficient fluorination (Figure 4g), while preserving the underlying Li crystal structure with minimal lattice disruption. Owing to this synergistic interfacial stabilization, Li|NCA88 with  $35 \mu\text{m}$  Li exhibited 82.4% capacity retention after 150 cycles. Zhang et al. incorporated 5 wt% of lithium tetrakis(perfluoro-tertbutyloxy)borate (Li-TFOB), a fluorine-rich borate ionic additive, into a 1 M  $\text{LiPF}_6$  EC/DMC electrolyte.<sup>[44]</sup> Due to its bulky size and weak coordinating nature, Li-TFOB undergoes preferential reduction during the initial cycles, facilitating the rapid formation of an inorganic bilayer SEI/CEI composed of LiF and Li—B—O species. This dual-layered interphase effectively stabilized Li deposition, reducing the overpotential in symmetric Li|Li cells from 125 to 25 mV over 1000 h and enhancing the CE of Li|Cu cells to 95% over 150 cycles. Furthermore, in high-voltage NMC622 full cells (4.6 V), the electrolyte exhibited an average CE of 99.1% and retained over 50% of the initial capacity after 500 cycles. Sung et al. employed silver trifluoromethanesulfonate ( $\text{AgCF}_3\text{SO}_3$ , AgTFMS) as a multi-functional additive to enable stable operation of ultrathin Li metal anodes ( $20 \mu\text{m}$ ).<sup>[45]</sup> Upon dissolution,  $\text{Ag}^+$  ions underwent in situ alloying with Li, forming a lithophilic Ag layer at the interface (Figure 4h), while the fluorine-rich  $\text{CF}_3\text{SO}_3^-$  anions contributed to the formation of a LiF-rich SEI. This dual interfacial protection layer of Ag and LiF lowered the nucleation overpotential (Figure 4i) and promoted uniform Li plating and reversible stripping, while also enhancing  $\text{Li}^+$  transport across the interface. Consequently, a  $20 \mu\text{m}$  Li|NMC811 full cell demonstrated excellent cycling stability with 88.2% capacity retention over 200 cycles (Figure 4j), underscoring the potential of this strategy toward practical implementation of ultrathin Li metal anode.

### 3. LMBs with SSEs

Commercial liquid electrolytes, due to their low viscosity and fast ion diffusion, promote localized lithium deposition, leading to dendrite formation and potential short circuits. Their flammable organic solvent base poses significant fire and explosion risks.

Moreover, with a limited electrochemical stability window (ESW) of around 4.2–4.3 V, they undergo oxidative decomposition when paired with high-voltage cathodes ( $\geq 4.4 \text{ V}$ ), reducing battery lifespan and efficiency.<sup>[46,47]</sup> To address these issues, SSEs have gained attention. Made from nonflammable solid materials, SSEs eliminate leakage and fire risks while their mechanical rigidity can suppress dendrite growth. With proper material design, SSEs can also offer a wider ESW, enabling compatibility with high-voltage cathodes. As a result, SSEs are considered a key technology for enabling high-energy, high-safety LMBs.

For SSEs to be applicable in practical batteries, they must meet several key requirements. First, they need sufficient ionic conductivity ( $\geq 10^{-4} \text{ S cm}^{-1}$  at room temperature) and ideally approach that of liquid electrolytes ( $\approx 10^{-3} \text{ S cm}^{-1}$ ) to ensure low resistance and fast charging. Second, a high lithium-ion transference number ( $t_{\text{Li}^+}$ ) is crucial to minimize concentration polarization and suppress dendrite growth. Third, mechanical strength is important—per Monroe and Newman's model, the shear modulus should be at least 1.8 times that of lithium metal ( $\approx 2\text{--}4 \text{ GPa}$ ) to block dendrite penetration.<sup>[48,49]</sup> Fourth, SSEs must maintain stable solid–solid interfaces with electrodes, accommodating volume changes and minimizing interfacial resistance and side reactions. Fifth, a wide ESW ( $\geq 0\text{--}4.5 \text{ V}$ ) is necessary for compatibility with lithium metal and high-voltage cathodes. Lastly, economic viability and ease of processing are essential for commercialization. This section evaluates polymer-based and inorganic ceramic-based SSEs against these benchmarks and introduces composite approaches that aim to combine their advantages.

#### 3.1. Polymer-Based SSEs

Polymer-based SSEs consist of a conductive polymer matrix and lithium salts, with ion transport occurring through polymer chain segmental motion. This process is more effective in amorphous polymers. These electrolytes offer flexibility, easy processing, and good electrode compatibility, but suffer from low room-temperature ionic conductivity, limited  $t_{\text{Li}^+}$  ( $<0.5$ ), and poor thermal/mechanical stability. Poly(ethylene oxide) (PEO) is the most studied but has notable limitations, leading to interest in alternatives like PVDF and PDOL. Devaux et al. designed and analyzed various block copolymer electrolytes to improve the trade-off between mechanical strength and ionic conductivity.<sup>[50]</sup> They found that a PS-PEO-PS triblock structure composed of 70% PEO and 30% PS exhibited the best performance, enabling stable, dendrite-free cycling for over 600 high-rate cycles.

Meanwhile, to overcome the intrinsic limitations of conventional PEO-based electrolytes—such as low  $t_{\text{Li}^+}$  ( $<0.2$ ), high-temperature dependence, and poor mechanical strength leading to dendrite penetration—various polymer designs have been proposed for single-ion conducting polymer electrolytes (SIPES) with immobilized anions. Bouchet et al. proposed a single-ion conducting BAB-type triblock copolymer electrolyte composed of a central PEO block and terminal P(STFSILi) blocks, where the  $\text{TFSI}^-$  anion is covalently immobilized (Figure 5a).<sup>[51]</sup> This design achieved a high  $t_{\text{Li}^+}$  ( $\approx 0.85$ ), effectively reducing

concentration polarization. Strong ionic cross-linking enhanced mechanical strength over 10-fold compared to PS-PEO-PS systems (Figure 5b). The electrolyte also exhibited high ionic conductivity of  $1.3 \times 10^{-5} \text{ S cm}^{-1}$  at  $60^\circ\text{C}$  (Figure 5c), a wide ESW ( $>5 \text{ V}$ ), and compatibility with high-voltage cathodes. In Li|SSE|LFP cells, it delivered stable cycling over 80 cycles at  $60\text{--}80^\circ\text{C}$ , maintaining  $>85\%$  capacity at C/2 and achieving  $138 \text{ mAh g}^{-1}$  at 2 C. Since SIPEs transport only lithium ions, they effectively suppress concentration polarization and inhibit dendrite growth. However, they still face challenges such as relatively low ionic conductivity ( $<10^{-5} \text{ S cm}^{-1}$ ) and practical  $t_{\text{Li}^+}$  values lower than expected due to ion aggregation. Bouchet et al. also noted that such anion aggregation can hinder  $\text{Li}^+$  hopping efficiency, particularly at lower temperatures, which represents a fundamental bottleneck for ion transport despite the immobilization of anions. To overcome these challenges, Cao et al. developed a SSE by blending an anion-immobilized copolymer, P(SSPSILi-alt-MA),

with a PEO matrix.<sup>[52]</sup> The MA units enhance salt dissociation and reduce PEO crystallinity, promoting ion transport. This design achieved high ionic conductivity ( $3.08 \times 10^{-4} \text{ S cm}^{-1}$  at room temperature), a  $t_{\text{Li}^+}$  of  $\approx 0.97$ , and excellent electrochemical stability—over 1300 h in Li|SSE|Li cells and 90% capacity retention after 350 cycles in Li|SSE|LFP cells. Han et al. demonstrated ambient-temperature all-solid-state lithium batteries using a sequence-controlled polymer (Alter-SIPE), where anionic units and PEO segments are alternately arranged along the backbone (Figure 5d,e).<sup>[53]</sup> This design suppresses ion aggregation and facilitates lithium-ion hopping along the chain. Simulations and electrochemical analysis confirmed lower Li–polymer binding energy, uniform ion distribution, and enhanced diffusion compared to conventional SIPEs. The optimized Alter-SIPE (P8) showed an ionic conductivity of  $4.2 \times 10^{-5} \text{ S cm}^{-1}$ ,  $t_{\text{Li}^+}$  of 0.93 at  $30^\circ\text{C}$ , and enabled over 1500 h of stable cycling in symmetric cells, with 99.3% Coulombic efficiency over 40 cycles in Li|SSE|LFP cells.

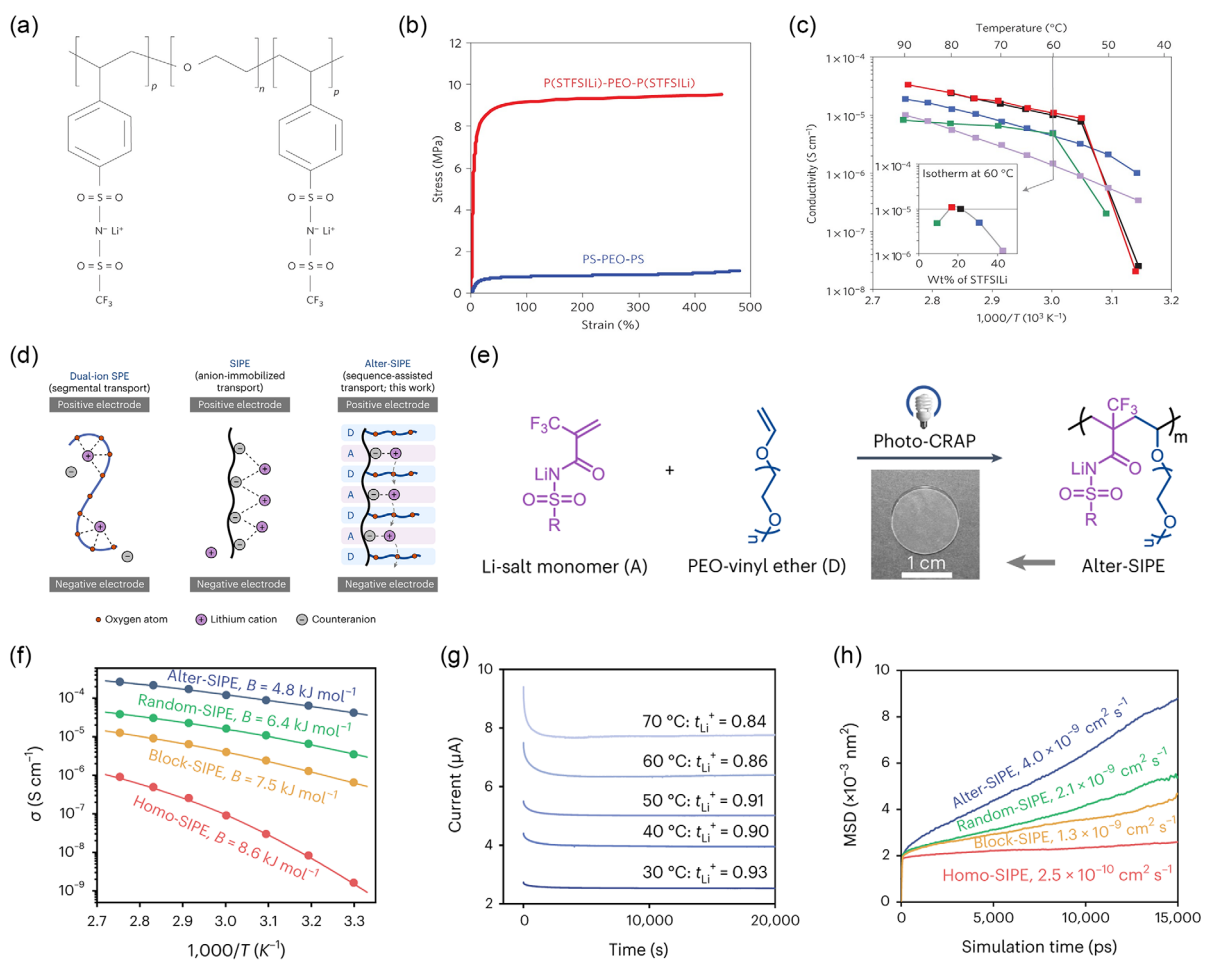


**Figure 5.** Design and performance of SIPEs: a) chemical structure of the triblock copolymer SIPE, P(STFSILi)-b-PEO-b-P(STFSILi), with covalently immobilized TFSI<sup>-</sup> anions. b) mechanical enhancement via ionic cross-linking in P(STFSILi)-PEO-P(STFSILi) compared to neutral PS-PEO-PS. c) ionic conductivity of SIPEs as a function of inverse temperature for various P(STFSILi)-PEO-P(STFSILi) copolymers; inset shows isothermal conductivity at  $60^\circ\text{C}$  versus P(STFSILi) content. Reproduced with permission.<sup>[51]</sup> Copyright 2013, Springer Nature. d) schematic comparison of ion transport in dual-ion versus single-ion polymer electrolytes. e) synthetic route of sequence-controlled Alter-SIPE via Photo-CRAP polymerization of electronic acceptor (A) and donor (D) monomers; inset shows a photograph of the resulting polymer. f) Vogel–Tammann–Fulcher plots of ionic conductivity for different SIPEs. B represents the pseudoactivation energy. g) investigation of  $t_{\text{Li}^+}$  with Alter-SIPE at varying temperature. h) MSD of Li<sup>+</sup> at  $30^\circ\text{C}$  for different SIPEs. Reproduced with permission.<sup>[53]</sup> Copyright 2023, Springer Nature.

(Figure 5f–h). Through such diverse molecular design strategies, SIEPs are increasingly recognized as a promising alternative to conventional polymer electrolytes, effectively mitigating inherent limitations such as low ionic conductivity and ion clustering.

To overcome the intrinsic limitation of low ionic conductivity exhibited by polymer-based SSEs at room temperature, quasi-SSEs (QSSEs) have emerged as an alternative, incorporating small amounts of organic solvents into the polymer matrix.<sup>[54–57]</sup> This strategy balances the mechanical flexibility and interfacial compatibility of polymers with liquid-like conductivity. PVDF-HFP-based electrolytes, known for their mechanical strength and stability but low conductivity, are widely used in QSSEs with added solvents.<sup>[57]</sup> However, their residual fluidity limits classification as true solid-state systems and raises concerns about solvent evaporation and long-term stability. To address this, solvent-free strategies have been pursued to realize high conductivity without the drawbacks of added liquids. One such example is poly(ionic liquid)-based electrolytes (PolyILs).<sup>[58]</sup> Wang X. et al. developed a solvent-free solid-state electrolyte system known as PolyILs-in-Salt, in which the PolyIL serves as the host matrix.<sup>[59]</sup> In this system, FSI<sup>-</sup> anions cocommorate with lithium ions and the polymer backbone, enabling efficient ion transport. The electrolyte achieved an ionic conductivity of  $0.7 \times 10^{-4}$  S cm<sup>-1</sup> and  $t_{Li^+}$  of 0.58 at 80 °C. Simulations and NMR confirmed fast ion transport, and the system showed excellent performance in LMBs, including over 500 h of stable cycling, 99.95% Coulombic efficiency, and 1.12 mAh cm<sup>-2</sup> capacity retention.

Recently, composite polymer electrolytes designed to suppress solvent fluidity while simultaneously achieving high ionic conductivity and electrochemical stability have garnered significant attention. Wang H. et al. developed a composite electrolyte, all-solid polyglycol oxide-based electrolyte, by immobilizing a deep eutectic solvent (DES) within a dual-cross-linked polymer network of PEGDA and UPyMA.<sup>[60]</sup> The N-methylurea-based DES with LiTFSI enhances lithium salt dissociation and forms strong hydrogen bonds with PEO, improving stability. This design eliminates solvent fluidity while achieving high ionic conductivity ( $3.42 \times 10^{-4}$  S cm<sup>-1</sup>), a wide ESW (5.2 V), and strong mechanical properties (17.6 MPa). The Li|SSE|LiCoO<sub>2</sub> cell retained 80% capacity after 1000 cycles at 4.6 V, reached 428.6 Wh kg<sup>-1</sup> in pouch format, and operated dendrite-free for over 2250 h. In another innovative approach, Zhang et al. developed a polymer blend composite electrolyte using ion-conductive PTFEP and mechanically robust PVDF-HFP, forming a single-phase, local-high-concentration solid electrolyte without phase separation.<sup>[61]</sup> The system maintains high local LiFSI concentration and continuous ion pathways, achieving an ionic conductivity of  $3.0 \times 10^{-4}$  S cm<sup>-1</sup>, oxidative stability >4.5 V, and dendrite suppression via LiF-rich SEI. Li|SSE|NMC811 cells cycled stably over 450 cycles at 4.5 V with 99.95% Coulombic efficiency, and pouch cells delivered ultrafast 4 C charging and >428.6 Wh kg<sup>-1</sup> energy density.

Polymer-based SSEs have emerged as promising candidates for all-solid-state Li metal batteries (ASSLMBs) due to their excellent processability and compatibility with electrode interfaces. Recently, extensive research has been conducted to overcome key limitations such as low ionic conductivity, dendrite

suppression, and electrochemical stability. Strategies including SIEPs, solvent-immobilized composite electrolytes, and single-phase polymer blend electrolytes have each addressed specific challenges, thereby significantly advancing the practical feasibility of polymer-based SSEs.

### 3.2. Inorganic Ceramic-Based SSEs

While polymer electrolytes enable lithium-ion transport via the segmental motion of polymer chains, inorganic ceramic-based SSEs conduct ions through a hopping mechanism along vacancies or interstitial sites within the crystal lattice. Efficient ionic transport depends on structurally continuous percolation pathways, which are influenced by the electrolyte's crystal structure and composition. Common inorganic ceramic SSEs, such as oxides and sulfides, allow selective lithium-ion conduction within a fixed anion lattice, typically achieving a much higher  $t_{Li^+}$  ( $\approx 1$ ) than polymer electrolytes. Inorganic ceramics are also known for their high ionic conductivity and mechanical strength, making them advantageous for suppressing lithium dendrites. However, recent studies have shown that mechanical strength alone is insufficient to fully prevent dendrite formation.<sup>[62]</sup> Residual electronic conductivity and unstable lithium stripping behavior at the interface are now recognized as key contributors. If the electrolyte conducts even a small number of electrons, lithium ions can be reduced within the bulk to form metallic lithium, initiating dendrites deep inside the material. Furthermore, rapid lithium stripping can lead to void formation at the interface, increasing local current density and promoting dendrite growth during subsequent plating steps, as described by the concept of critical stripping current (Figure 6a).<sup>[63]</sup> In addition to electrochemical instability, inorganic ceramic-based SSEs face challenges such as the use of costly raw materials, the need for high manufacturing costs associated with high-temperature sintering processes, and relatively poor interfacial stability with electrodes due to their rigid nature compared to polymer-based SSEs. Therefore, practical application of inorganic ceramic-based SSEs requires integrated materials and process design that comprehensively addresses both electrochemical and interfacial stability.

#### 3.2.1. Oxide-Based SSEs

Oxide-based SSEs have attracted significant attention as next-generation electrolytes for all-solid-state batteries due to their high ionic conductivity ( $10^{-4}$ – $10^{-3}$  S cm<sup>-1</sup>),  $t_{Li^+} \approx 1$ , and excellent thermal and chemical stability. Representative examples include garnet-type Li<sub>7</sub>La<sub>3</sub>Zr<sub>2</sub>O<sub>12</sub> (LLZO) and NASICON-type materials such as Li<sub>1+x</sub>Al<sub>x</sub>Ti<sub>2-x</sub>(PO<sub>4</sub>)<sub>3</sub> (LATP) and Li<sub>1+x</sub>Al<sub>x</sub>Ge<sub>2-x</sub>(PO<sub>4</sub>)<sub>3</sub> (LAGP). Both material classes face challenges in maintaining interfacial stability with electrodes. In particular, LATP and LAGP exhibit significant interfacial resistance due to their high reactivity with lithium metal. By contrast, LLZO is chemically stable upon direct contact with lithium metal, but at room temperature, it tends to form a tetragonal phase with relatively low ionic conductivity compared to other oxide-based electrolytes. To address this,

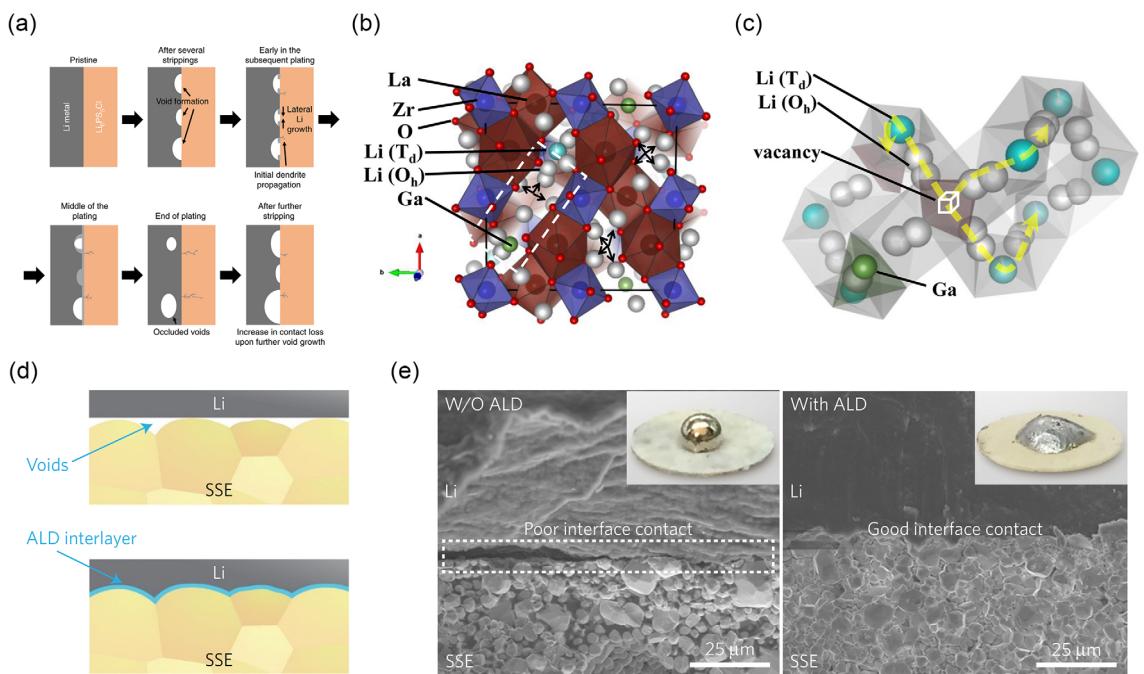


**Figure 6.** Interfacial and structural engineering strategies for oxide-based SSEs. a) Schematic sequence showing void formation and occlusion during repeated lithium stripping and plating at the interface of inorganic ceramic SSEs, leading to contact loss and dendrite growth. Reproduced with permission.<sup>[63]</sup> Copyright 2019, Springer Nature. b) Garnet structure of  $\text{La}_3\text{Zr}_2\text{Li}_{7-3x}\text{Ga}_x\square_2\text{O}_{12}$  where the blue circles are Zr in octahedral ( $\text{O}_h$ ) coordination, the dark red circles are La in dodecahedral coordination, the gray circles are Li in  $\text{O}_h$  coordination, the turquoise blue and green circles are Li and Ga in tetrahedral ( $\text{T}_d$ ) coordination, respectively, and the arrows represent a vacancy ( $\square$ ). c) Vacancy representation ( $\square$ ) of an enlarged area of (a) (dotted lines) showing the Li pathway in the garnet structure. Reproduced with permission.<sup>[67]</sup> Copyright 2014, American Chemical Society. d) Schematic illustration of molten lithium wetting behavior on garnet surfaces, with and without ALD- $\text{Al}_2\text{O}_3$  coating. e) Cross-sectional SEM images demonstrating improved interfacial contact between Li metal and garnet SSE after ALD treatment; insets show enhanced wetting behavior on coated surfaces. Reproduced with permission.<sup>[18]</sup> Copyright 2017, Springer Nature.

researchers have doped LLZO with higher-valent cations such as  $\text{Ta}^{5+}$  or  $\text{Nb}^{5+}$  to expand lithium-ion pathways and stabilize the highly conductive cubic phase.<sup>[64–66]</sup> Li et al. demonstrated that  $\text{Ta}^{5+}$ -doped LLZO, specifically at the composition  $\text{Li}_{6.4}\text{La}_3\text{Zr}_{1.4}\text{Ta}_{0.6}\text{O}_{12}$  ( $x = 0.6$ ), achieves a room-temperature ionic conductivity of  $1.0 \times 10^{-3} \text{ S cm}^{-1}$  and a low activation energy of 0.35 eV, identifying the optimal vacancy concentration through a volcano-type plot.<sup>[65]</sup> Meanwhile, Bernuy-Lopez et al. used  $\text{Ga}^{3+}$  doping in place of  $\text{Zr}^{4+}$  to introduce lithium vacancies and performed sintering under dry oxygen conditions to suppress moisture-induced degradation, stabilizing the cubic phase (Figure 6b,c).<sup>[67]</sup> This approach yielded a high ionic conductivity of  $1.3 \times 10^{-3} \text{ S cm}^{-1}$  at room temperature for  $\text{La}_3\text{Zr}_2\text{Li}_{7-3x}\text{Ga}_x\text{O}_{12}$  ( $x = 0.15$ ). Multielement doping (e.g., Ta–Al) is also being explored to further enhance cubic phase stability.<sup>[66]</sup> However, these doping strategies often create lithium-deficient compositions, which can lead to the formation of interfacial resistance layers or structural degradation of the electrolyte upon contact with lithium metal, ultimately reducing battery lifespan or causing short circuits. In addition, excessive  $\text{Li}^{+}$  vacancies may trigger electronic conduction, providing pathways for internal dendrite formation and compromising long-term stability. To overcome these limitations, Jung et al. proposed a full-lithium composition ( $\text{Li} = 7.0$ ) combined with a high-entropy doping strategy, enabling stable cubic phase formation without lithium vacancies

and significantly enhancing reduction stability against lithium metal.<sup>[68]</sup> By codoping  $\text{Zr}^{4+}$  sites with elements such as Hf, Sn, Sc, and Ta, they achieved room temperature cubic stability and successful synthesis at low temperatures ( $\approx 400^\circ\text{C}$ ). The resulting garnet electrolyte exhibited excellent long-term interfacial stability with lithium metal and retained 92% of its initial capacity after 700 cycles in a quasi-all-solid-state cell, demonstrating strong practical potential. In a parallel study, Feng et al. synthesized high-entropy oxide-based garnets via ultrafast high-temperature sintering, completing the process in just a few tens of seconds.<sup>[69]</sup> This approach significantly reduced processing time while improving manufacturing efficiency. Their electrolyte exhibited an ionic conductivity of  $3.57 \times 10^{-4} \text{ S cm}^{-1}$  and a high critical current density of  $2.4 \text{ mA cm}^{-2}$ , along with a very low electronic conductivity ( $5.26 \times 10^{-9} \text{ S cm}^{-1}$ ), which correlates with suppressed  $\text{Li}^{+}$  vacancy-related conduction pathways. The entropy stabilization effect not only enhanced the structural stability of the cubic phase but also contributed to the dendrite suppression, likely associated with reduced electronic conduction.

In addition to doping and compositional tuning strategies aimed at enhancing ionic conductivity, interfacial stability with electrodes has emerged as another critical challenge for oxide-based SSEs.<sup>[70]</sup> In the case of LLZO, voids tend to form at the solid–solid interface with lithium metal, and contamination layers such as  $\text{Li}_2\text{CO}_3$  and  $\text{LiOH}$  reduce wettability, resulting in high

interfacial resistance. Sharafi et al. identified this issue and demonstrated that wet polishing followed by thermal treatment could effectively remove these surface contaminants, achieving an ultra-low interfacial resistance of  $\approx 2 \Omega \text{ cm}^2$ .<sup>[71]</sup> Han et al. applied an atomic layer deposition (ALD) technique to coat the surface of a doped garnet electrolyte, LLCZN ( $\text{Li}_7\text{La}_{2.75}\text{Ca}_{0.25}\text{Zr}_{1.75}\text{Nb}_{0.25}\text{O}_{12}$ ), with a thin  $\text{Al}_2\text{O}_3$  film (Figure 6d).<sup>[18]</sup> This coating effectively suppressed void formation and  $\text{Li}_2\text{CO}_3$  accumulation at the Li interface, significantly improving wettability (Figure 6e). As a result, the interfacial resistance was dramatically reduced from  $1710 \Omega \text{ cm}^2$  to just  $1 \Omega \text{ cm}^2$ , which was attributed to the formation of a Li—Al—O interphase with high ionic conductivity and excellent chemical stability. While LATP and LAGP generally exhibit higher ionic conductivity than LLZO, they suffer from severe interfacial degradation when in direct contact with lithium metal. In such cases,  $\text{Ti}^{4+}$  or  $\text{Ge}^{4+}$  ions are reduced, leading to the formation of undesired interphases that significantly increase interfacial resistance. To mitigate this, Cheng et al. introduced a nanocomposite coating of boron nitride less than 10 nm thick on the LATP surface.<sup>[72]</sup> This coating prevented direct chemical contact with lithium and maintained high interfacial stability, achieving 96.6% capacity retention after 500 charge/discharge cycles. In a different approach, Liu et al. inserted a high-conductivity plastic-crystalline interlayer (I-SN) containing LLZAO nanowires between the lithium metal and LAGP, using an *in situ* solidification method.<sup>[73]</sup> This strategy effectively suppressed interfacial reactions and maintained stable interfacial resistance, enabling reliable dendrite suppression, high-rate cycling, and long-term performance (93.17% capacity retention after 100 cycles). Additionally, since oxide-based SSEs generally require high-temperature sintering, active research is ongoing to simplify and optimize their processing conditions.<sup>[74,75]</sup>

Oxide-based SSEs offer key advantages such as high ionic conductivity ( $10^{-4}$ – $10^{-3} \text{ S cm}^{-1}$ ), wide ESW, and excellent thermal and chemical stability, making them strong candidates for next-generation ASSLMBs. However, issues like poor interfacial contact, interfacial reactivity, and high-temperature sintering still limit practical application. Recent progress in doping, interface engineering, and low-temperature synthesis shows promise, but further efforts are required to improve interfacial stability and enable scalable, cost-effective processing. Future research should integrate materials design with manufacturability to fully realize their potential.

### 3.2.2. Sulfide-Based SSEs

Sulfide-based SSEs exhibit  $t_{\text{Li}^+}$  close to 1 and achieve high ionic conductivities ( $10^{-3}$ – $10^{-2} \text{ S cm}^{-1}$ ) at room temperature, comparable to or even exceeding those of liquid electrolytes. Unlike oxide-based SSEs, sulfide electrolytes are mechanically ductile, enabling better interfacial contact with electrodes and allowing room-temperature processing.<sup>[76]</sup> Due to these advantages, various types of sulfide-based SSEs have been developed, including glassy ( $\text{Li}_2\text{S}-\text{SiS}_2$ ), glass-ceramic ( $\text{Li}_2\text{S}-\text{P}_2\text{S}_5$ ), crystalline argyrodite ( $\text{Li}_6\text{PS}_5\text{Cl}$ ), and LGPS ( $\text{Li}_{10}\text{GeP}_2\text{S}_{12}$ ) systems.<sup>[77]</sup> However, sulfide-based SSEs also face challenges, such as chemical reactivity with

electrodes, extreme moisture sensitivity, and narrow ESW, which often lead to interfacial resistance buildup and reduced cycle life. Notably, interfacial decomposition with lithium metal, space-charge layer formation at cathode interfaces, and lithium dendrite growth during cycling are major interfacial challenges. Consequently, extensive research has focused on analyzing and stabilizing these interfaces.<sup>[78–82]</sup> Takada et al. introduced a  $\text{LiNbO}_3$  nanocoating ( $\leq 20 \text{ nm}$ ) on spinel  $\text{LiMn}_2\text{O}_4$  cathodes, which suppressed space-charge layers and reduced interfacial resistance from  $\approx 10\,000$  to  $\approx 200 \Omega$ , significantly enhancing interface stability.<sup>[78]</sup> Wang et al. inserted a succinonitrile-based PCE protection layer between LGPS and lithium metal (Figure 7a), blocking side reactions and reducing overpotential from 750 to 40 mV.<sup>[83]</sup> Additionally, efforts have also been made to modify the electrolyte composition and crystal structure via doping or substitution to intrinsically mitigate interfacial reactivity.<sup>[84–86]</sup> For example, Zhao et al. partially substituted  $\text{P}^{5+}$  with  $\text{Sn}^{4+}$  in argyrodite-type  $\text{Li}_6\text{PS}_5\text{I}$  (Figure 7b,c), expanding the lattice and increasing  $\text{Li}^+$  content, which enhanced ionic conductivity to  $3.5 \times 10^{-4} \text{ S cm}^{-1}$ —125 times higher than the undoped version.<sup>[87]</sup> The Sn—S bond formed a self-passivating SEI layer, enabling stable Li plating/stripping at  $1.26 \text{ mA cm}^{-2}$  for over 200 h, while also preserving the crystal structure after air exposure. More recently, Li et al. proposed a stress self-constraining mechanism using a blended LPSCl—LGPS electrolyte to form a dynamically stabilized mixed conductive interface.<sup>[88]</sup> The volume expansion of early decomposition products generated compressive stress that suppressed further breakdown, resulting in over 1500 h of stable Li plating/stripping, 22.6 GPa mechanical strength, 93.7% capacity retention after 100 cycles, and uniform lithium deposition. Furthermore, dual-interface stabilization strategies that combine composite anodes with doped electrolytes have also been reported to enable uniform Li deposition and effective dendrite suppression.<sup>[89]</sup>

One of the major drawbacks of sulfide-based SSEs is their extreme sensitivity to moisture in the air. Upon exposure to atmospheric moisture, they undergo hydrolysis and release hydrogen sulfide gas ( $\text{H}_2\text{S}$ ), which is toxic to humans. Hence, improving air stability has become a critical research objective. For instance, Muramatsu et al. systematically studied various  $\text{Li}_2\text{S}-\text{P}_2\text{S}_5$  compositions, analyzing structural changes and  $\text{H}_2\text{S}$  evolution.<sup>[90]</sup> They found that the 75  $\text{Li}_2\text{S}$ –25  $\text{P}_2\text{S}_5$  composition produced the least  $\text{H}_2\text{S}$  while maintaining stable structural integrity and ionic conductivity ( $1.9 \times 10^{-4} \text{ S cm}^{-1}$ ), indicating its promise as an air-stable SSE candidate. In addition to such compositional optimization, the intrinsic bonding nature also governs the air stability of sulfide electrolytes. For example, LGPS can suffer more severe hydrolysis because Ge—S bonds are relatively weaker and more susceptible to water attack, while  $\text{Li}_6\text{PS}_6\text{Cl}$  shows comparatively better air stability due to its stronger P—S bonds and the stabilizing effect of  $\text{Cl}^-$ , which helps inhibit hydrolysis.<sup>[91,92]</sup> To overcome these limitations, surface coating technologies have been developed to enhance the air stability of sulfide electrolytes. For example, Hood et al. applied multifunctional  $\text{Al}_2\text{O}_3$ -based coatings on sulfide electrolyte powders, which improved moisture resistance, suppressed  $\text{H}_2\text{S}$  release, and enhanced stability under ambient conditions.<sup>[93]</sup> Similarly,

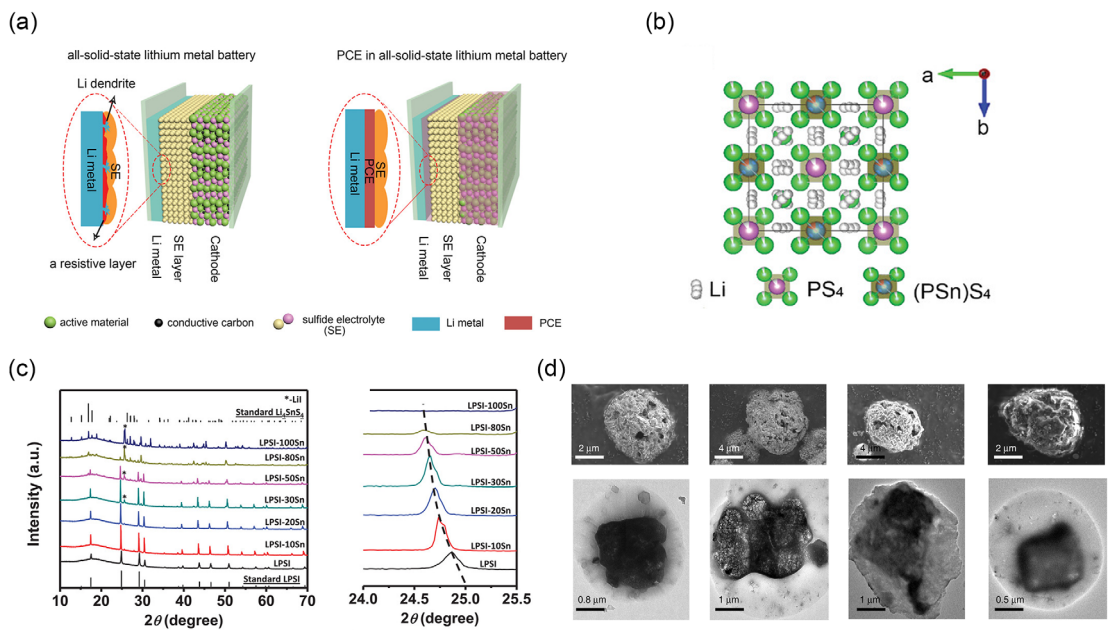


**Figure 7.** Interface stabilization and structural modification strategies for sulfide-based SSEs. a) Schematic comparison of conventional ASSLMBs and those incorporating a PCE interlayer for improved interface stability. Reproduced with permission.<sup>[83]</sup> Copyright 2019, Wiley-VCH. b) Structure of the prepared LPSI-xSn ( $\text{Li}_{6.24}\text{P}_{0.823}\text{Sn}_{0.177}\text{S}_{4.580.9}$ ) from the view of perpendicular to c-axis. c) XRD patterns of LPSI-xSn electrolytes ( $x = 0, 10, 20, 30, 50, 80, 100$ ). right: Magnified region of the XRD patterns in the  $2\theta$  range:  $24^\circ < 2\theta < 25.5^\circ$ . Reproduced with permission.<sup>[87]</sup> Copyright 2020, Wiley-VCH. d) SEM and TEM images of LPSI-xSn powders annealed at 450, 460, 480, and 500 °C, revealing core–shell microstructures correlated with thermal processing. Reproduced with permission.<sup>[96]</sup> Copyright 2018, Springer Nature.

Jung et al. reported a core–shell architecture in which a thin oxy-sulfide nanolayer was formed on  $\text{Li}_6\text{PS}_5\text{Cl}$  particles, effectively acting as a moisture barrier and reducing degradation while maintaining high ionic conductivity.<sup>[94]</sup> To enhance air stability further, Liang et al. substituted part of the  $\text{P}^{5+}$  in LGPS with  $\text{Sb}^{5+}$ , producing  $\text{Li}_{10}\text{Ge}(\text{P}_{1-x}\text{Sb}_x)\text{S}_{12}$ .<sup>[95]</sup> This modification boosted ionic conductivity to  $17.3 \text{ mS cm}^{-1}$ , retained  $15.7 \text{ mS cm}^{-1}$  after air exposure, suppressed  $\text{H}_2\text{S}$  evolution, and ensured structural robustness—demonstrating a significant improvement in atmospheric stability. This indicates that doping, used earlier for interfacial stabilization, is also an effective strategy for enhancing air stability. Another critical limitation of sulfide electrolytes is their narrow ESW, which leads to oxidation and degradation at high voltages. To address this, Wu et al. introduced a core–shell structure into LSPS-based electrolytes (Figure 7d).<sup>[96]</sup> This extended the stability window from 1.7–2.1 V to  $\approx 0.7$ –3.1 V, and thanks to a Si-rich rigid amorphous shell that suppresses volume expansion through a “volume constriction” mechanism, the electrolyte was demonstrated (through both experiments and DFT calculations) to function stably up to 5 V. Alongside these advances in stability, efforts to optimize production processes are also in progress.<sup>[97]</sup> For example, LGPS contains germanium (Ge), a rare and costly element that limits scalability. Substituting or eliminating Ge with alternatives such as Si or Sn—while maintaining comparable ionic conductivity—has become a key research direction.<sup>[98,99]</sup> Meanwhile, Li et al. developed  $\text{Li}_7\text{P}_3\text{S}_{7.5}\text{O}_{3.5}$  (LPSO) using low-cost  $\text{Li}_2\text{O}$  and  $\text{P}_2\text{S}_5$  instead of expensive  $\text{Li}_2\text{S}$ .<sup>[100]</sup> LPSO offers low cost ( $\approx 14.4 \text{ USD kg}^{-1}$ ), low density ( $1.70 \text{ g cm}^{-3}$ ), high ionic conductivity ( $4.58 \times 10^{-4} \text{ S cm}^{-1}$ ), and excellent interfacial compatibility with lithium metal and silicon

anodes. It demonstrated stable performance over 4,200 h in symmetric cells and over 200 cycles in pouch cells, marking a significant step toward practical implementation.

Sulfide-based SSEs are promising for high-performance ASSLMBs due to their high ionic conductivity (up to  $10^{-2} \text{ S cm}^{-1}$ ) and excellent deformability, enabling intimate electrode contact and room-temperature processing. However, challenges such as moisture sensitivity, narrow ESW, and poor interfacial compatibility limit their practical use. While recent advances in surface coating, doping, interface engineering, and air-stable composites have addressed some of these issues, further efforts are needed to improve long-term stability, safety, and scalability. Future research should focus on integrating materials innovation with practical cell design and manufacturing strategies to realize their commercial potential.

### 3.3. Composite SSEs

Composite SSEs combine materials with differing properties to address the limitations of single-phase electrolytes. They include polymer/polymer, inorganic/inorganic, and inorganic/polymer systems. Among these, inorganic/polymer composites are especially promising, as they balance polymer flexibility and interfacial adaptability with the high conductivity and mechanical strength of ceramics.

Inorganic filler-based polymer electrolytes represent one of the most actively explored directions among composite SSEs. This approach involves incorporating inorganic fillers (e.g., ceramic nanoparticles, nanowires) into a polymer matrix to

suppress polymer crystallization and expand the amorphous region, thereby enhancing lithium-ion mobility. Additionally, the inorganic fillers themselves can provide supplementary ionic conduction pathways. A representative example is the work by Liu et al., who aligned LLTO nanowires along the electrode direction within a PAN matrix, enabling lithium ions to migrate along uninterrupted straight pathways (Figure 8a,b).<sup>[101]</sup> This design achieved a room temperature ionic conductivity of  $6.05 \times 10^{-5} \text{ S cm}^{-1}$ , over 10 times higher than that of a randomly dispersed system. X-ray diffraction (XRD) and conductivity

analyses confirmed that the conductivity enhancement was attributed to surface conduction along the aligned fillers rather than changes in crystallinity. Similarly, Zhang et al. developed a freestanding composite electrolyte by blending Li<sub>6</sub>PS<sub>5</sub>Cl particles, a PEO-based polymer, and an ionic liquid, forming a self-supporting membrane via solvent casting without a substrate.<sup>[102]</sup> The composite exhibited high room-temperature ionic conductivity ( $1.4 \times 10^{-3} \text{ S cm}^{-1}$ ) and good interfacial contact, enabling stable Li|SSE|LiCoO<sub>2</sub> cell operation for over 100 cycles—demonstrating the potential of flexible, practical SSEs. Hu et al. applied a

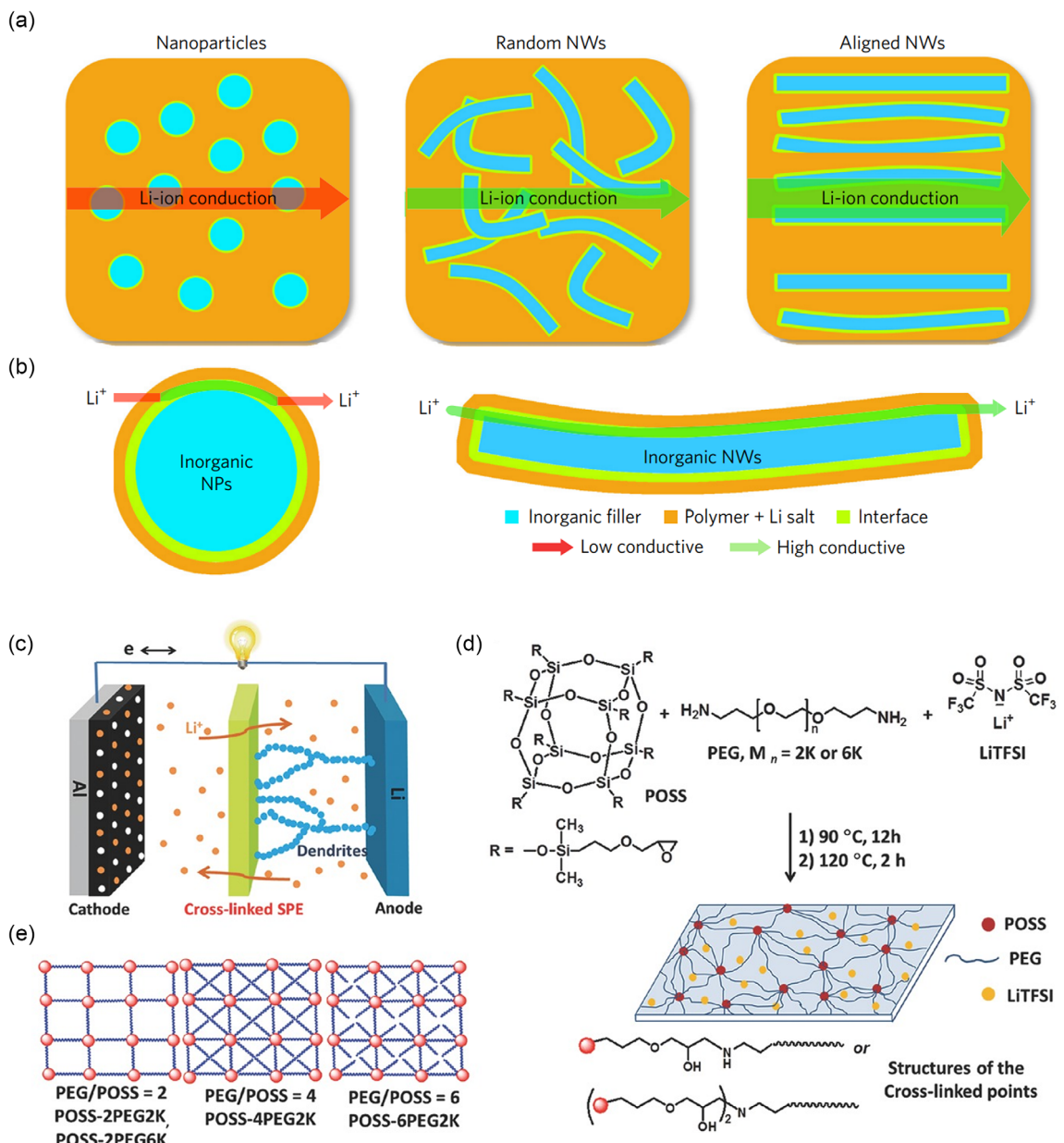


**Figure 8.** Structural design strategies for polymer/inorganic composite SSEs. a) Li-ion conduction pathways in composite electrolytes with nanoparticles, randomly oriented nanowires, and aligned nanowires. Aligned nanowires enable uninterrupted conduction without crossing junctions. b) Schematic representation of the highly conductive interfacial regions surrounding inorganic nanoparticles and nanowires embedded in polymer matrices. Reproduced with permission.<sup>[101]</sup> Copyright 2017, Springer Nature. c) Schematic illustration of a LMB with a cross-linked POSS-PEO SPE as separator to block the growth of lithium dendrites. d) Synthesis of the POSS-PEO cross-linked SPEs ( $\text{EO/Li}^+ = 16$ ) and e) the ideal structures of the networks. Reproduced with permission.<sup>[105]</sup> Copyright 2015, Wiley-VCH.

dual-fluorination strategy to a PEO-based polymer electrolyte combined with a conversion-type  $\text{FeF}_3$  cathode, resulting in a  $t_{\text{Li}^+}$  of 0.67, stable SEI formation, and improved cathode reversibility.<sup>[103]</sup> The incorporated HS-AlF<sub>3</sub> filler served multiple roles—ionic conduction, interfacial stabilization, and fluorine enrichment—leading to over 900 stable cycles and high-rate performance exceeding 260 mAh g<sup>-1</sup> at 3500 mA g<sup>-1</sup>. Additionally, Wu et al. improved PVDF-based polymer SSEs by incorporating MoSe<sub>2</sub> nanosheets via a phase regulation strategy.<sup>[104]</sup> The fillers enhanced electrolyte densification, induced  $\beta$ -phase transition, and formed a Li<sub>2</sub>Se-based SEI in situ. This resulted in high ionic conductivity ( $6.4 \times 10^{-4}$  S cm<sup>-1</sup>), excellent cycling stability over 2000 cycles, and strong performance at high areal loading (2.6 mAh cm<sup>-2</sup>) and rate (3 C).

While inorganic-filler-based polymer electrolytes have improved ionic conductivity and interfacial stability through relatively simple designs, their practical performance is still constrained by nonuniform filler dispersion and a lack of structural continuity. To overcome these issues, an alternative approach involves forming a continuous inorganic network structure within the polymer matrix. By strengthening connectivity between inorganic domains through physical or chemical bonding, such hybrid architectures aim to enhance ion-transport pathways while simultaneously reinforcing mechanical integrity. Pan et al. exemplified this concept by developing a 3D hybrid electrolyte using polyhedral oligomeric silsesquioxane (POSS) nanoclusters as nanoscale cross-linkers and polyethylene glycol (PEG) chains as the conductive matrix in a one-pot step synthesis (Figure 8c,d).<sup>[105]</sup> By adjusting the POSS-to-PEG ratio (Figure 8e), they achieved both a high storage modulus and a room-temperature ionic conductivity of  $\geq 10^{-4}$  S cm<sup>-1</sup>. The electrolyte enabled stable Li|SSE|Li cycling for 2600 h at 0.3 mA cm<sup>-2</sup>, suppressed dendrites at 1 mA cm<sup>-2</sup>, and maintained over 99% Coulombic efficiency in LiFePO<sub>4</sub> cells after 50 cycles. Addressing the long-standing trade-off between mechanical robustness and conductivity from a different perspective, Choudhury et al. designed a crosslinked nanoparticle-polymer composite incorporating a small amount of liquid electrolyte.<sup>[106]</sup> Hairy silica nanoparticles bearing PEO chains were chemically cross-linked with PPO chains to form a 3D scaffold that imbibes the liquid phase. The resulting membrane a solid-like modulus ( $> 10^6$  Pa) and high conductivity ( $1.3 \times 10^{-3}$  S cm<sup>-1</sup>), enabling stable Li|SSE|Li cycling for over 500 h and retaining  $> 90\%$  capacity in Li<sub>4</sub>Ti<sub>5</sub>O<sub>12</sub> cells after 150 cycles. Together, these studies highlight continuous inorganic networking and hybrid quasi-solid designs as promising routes for advancing composite SSEs beyond the limitations of conventional filler dispersion.

In addition to structural design, composite SSEs are increasingly engineered to meet diverse functional demands such as mechanical strength, interfacial stability, high-voltage compatibility, and scalable processability. For mechanical enhancement, Li A. et al. developed a nacre-inspired LAGP-polymer laminate showing high flexural strength (7.8 GPa) and good ionic conductivity ( $\approx 10^{-4}$  S cm<sup>-1</sup>), with stable cycling under compression and at 60 °C.<sup>[107]</sup> To improve interfacial stability, Wang et al. designed a 3D Li<sub>6</sub>PS<sub>5</sub>Cl scaffold with in situ polymerized monomers, achieving  $4.6 \times 10^{-4}$  S cm<sup>-1</sup> conductivity and over 500 h of Li|SSE|Li

cycling.<sup>[108]</sup> For high-voltage operation, Li Z. et al. used LAGP-coated LiCoO<sub>2</sub> and a mixed-salt electrolyte to suppress PEO degradation, retaining 81.9% capacity after 400 cycles at 4.25 V.<sup>[109]</sup> Lastly, Guo et al. created a flexible, slurry-processable LAGP-based composite compatible with various cathodes, supporting cost-effective scale-up.<sup>[110]</sup> These studies highlight how targeted strategies are broadening the functional capabilities of composite SSEs.

Composite SSEs offer a promising solution to the limitations of single-phase electrolytes by combining polymer flexibility with the conductivity and strength of ceramics. Advances in filler design and structure have improved conductivity, mechanical properties, and high-voltage stability, enabling strong room-temperature performance and long cycle life. However, challenges like interfacial inhomogeneity, filler dispersion, and fabrication complexity remain. Future work should prioritize integrated, scalable designs to support commercial adoption of ASSLMBs.

## 4. Conclusion and Perspectives

This review is dedicated to electrolyte design for LMBs, presenting a systematic and comprehensive analysis of principal strategies in both liquid and SSE systems. In the liquid electrolyte section, we examine three directions: HCEs/LHCEs for inorganic-rich SEI formation with reduced viscosity; fluorinated solvents/salts for enhanced stability and Al-corrosion suppression; and functional additives for tailored interfacial chemistry and engineered SEI/CEI. In the SSE section, we explore advances in polymer-based, inorganic ceramic, and composite electrolytes. Key strategies include molecular design for enhanced ion transport in polymers, doping and interface engineering for ceramics, and hybrid architectures that combine mechanical strength with interfacial stability. Building on the insights discussed above, we outline future research directions that aim to enable more strategic and precise electrolyte design for LMBs (Figure 9).

For liquid electrolytes, the development of LHCEs remains one of the most promising strategies for practical LMBs. By combining the interfacial stability of high-concentration systems with improved viscosity and ionic conductivity, LHCEs offer a balanced pathway toward scalability and safety. Nevertheless, their long-term thermal stability, cost, and compatibility with high-voltage cathodes require further optimization. In parallel, recent studies have also revisited electrolytes with salt concentrations lower than the conventional 1 M baseline, aiming to simultaneously reduce viscosity and cost while maintaining interfacial stability through tailored solvent-anion coordination.<sup>[111]</sup> These emerging directions highlight that, beyond simply tuning concentration, the rational design of solvent-salt-diluent interactions will be critical to achieve electrolytes capable of supporting stable Li cycling under realistic conditions. Moreover, recent studies have underscored the renewed importance of inorganic additives in stabilizing electrode-electrolyte interfaces. By incorporation inorganic fluorides or complex metal fluorides such as Li<sub>2</sub>ZrF<sub>6</sub>, these systems promote the formation of robust, inorganic-rich interphases,

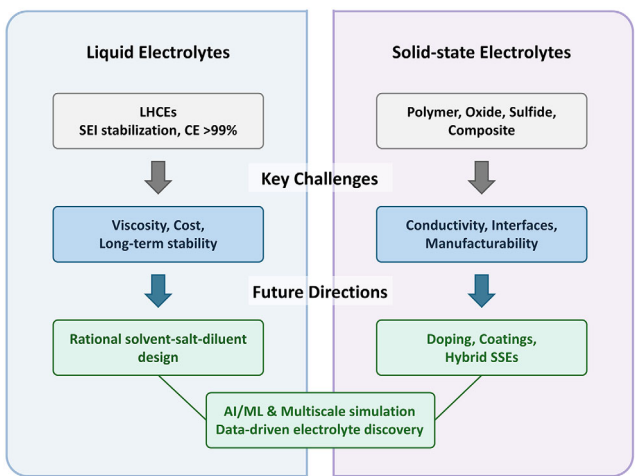


**Figure 9.** Summary of current strategies, key challenges, and future directions for liquid electrolytes (LHCEs) and SSEs.

offering complementary benefits to solvent-salt engineering strategies for liquid electrolyte.<sup>[112,113]</sup>

For SSEs, several key future directions can be identified. Improving room-temperature ionic conductivity remains a central challenge, requiring new design strategies for polymers, ceramics, and their composites. Stabilizing interfaces with lithium metal and high-voltage cathodes is another critical goal, which may be achieved through advanced coatings, interfacial buffer layers, or engineered composite architectures. Composite SSEs that integrate polymer flexibility with ceramic strength also represent a promising pathway, particularly when combined with scalable fabrication methods. In addition, enhancing the environmental and chemical stability of sulfide-based electrolytes and minimizing reliance on scarce elements such as Ge will be essential to ensure sustainability. Beyond these scientific directions, practical considerations must also be addressed for successful commercialization. Priorities include lowering production costs by adopting abundant raw materials and reducing the energy demand of ceramic processing through low-temperature or ultra-fast sintering of garnet-type LLZO. Compatibility with existing electrode fabrication and roll-to-roll assembly processes will be vital to facilitate industrial adoption, while establishing standardized safety assessment protocols—including mechanical abuse, thermal runaway, and short-circuit tolerance—will provide reliable benchmarks for commercialization of next-generation solid-state LMBs.

In addition to these practical considerations, computational and theoretical studies are also crucial for guiding the rational design of next-generation electrolytes. First, it is essential to expand DFT and ab-initio molecular dynamics (AIMD)-based studies to provide atomic-level resolution in elucidating electrolyte systems, including Li<sup>+</sup> ion solvation structures and ion conduction mechanisms.<sup>[114]</sup> Moreover, atomic-scale elucidation of the electron transfer processes, ionic transport behaviors, and initial SEI formation mechanisms at the electrolyte-Li metal interface will allow the identification of root causes governing interfacial stability. In addition, electrochemical stability data can also be

established by evaluating the electrochemical window of solid electrolytes and calculating the HOMO and LUMO levels of organic electrolytes.<sup>[115]</sup>

Second, to extend the high-fidelity insights gained from quantum mechanics to larger, more complex systems, it is essential to bridge the gap between atomic-scale accuracy and the demands of mesoscopic simulations. Machine learning interatomic potentials (MLIPs) have emerged as a transformative tool for this purpose. By learning from extensive DFT datasets, MLIPs can reproduce quantum-level accuracy while enabling large-scale MD simulations with computational efficiency comparable to that of classical force fields, thereby facilitating the upscaling of atomic-level understanding to multiscale modeling frameworks. Leveraging MLIPs, it becomes possible to simulate the formation of SEI at the atomic and molecular level, offering insights inaccessible to experimental techniques. Such MLIP simulations are expected to provide valuable guidance for more refined and strategic electrolyte design.

Third, to accelerate the discovery of next-generation electrolytes, it is essential to build an integrated, large-scale database that encompasses experimental observations, first-principles (DFT/AIMD) results, and large-scale MLIP-based simulations.<sup>[116]</sup> By leveraging machine learning models trained on such multi-source data, it becomes possible to perform high-throughput screening<sup>[117]</sup> and identify electrolyte candidates optimized for a balanced combination of electrochemical stability, ionic conductivity, and safety. A wide range of data is continuously being accumulated, spanning from ionic conductivity<sup>[118]</sup> to experimentally measured Coulombic efficiency<sup>[119]</sup> and cycling performance.<sup>[120]</sup> Importantly, this computational and experimental data-driven strategy can extract relationships between materials, processes, and properties across multiple scales, from atomic-level interactions to mesoscale interfacial behavior, and, leveraging generative AI techniques, efficiently guide the design toward practically applicable new formulations. The synergistic integration of these three strategic directions is expected to play a pivotal role in overcoming the remaining scientific and technological barriers in electrolyte design, ultimately accelerating the realization of high-performance and safe next-generation LMBs.

## Acknowledgements

This research was supported by the Nano & Material Technology Development Program through the National Research Foundation of Korea (NRF) funded by Ministry of Science and ICT (RS-2024-00448287). Also, this work was supported by the National Research Foundation of Korea Grant funded by the Korean Government (RS-2024-00414824). European Regional Development Fund <http://dx.doi.org/10.13039/501100008530> (2022 FGI 0007).

## Conflict of Interest

The authors declare no conflict of interest.

## Author Contributions

**Un Hwan Lee:** conceptualization (equal); data curation (lead); validation (lead); visualization (lead); writing—original draft (lead). **Seonhye Park:** data curation (equal); validation (equal); visualization (equal); writing—original draft (equal). **Joonhee Kang:** conceptualization (lead); project administration (lead); supervision (lead); writing—review & editing (lead). U.H.L. and S.P. contributed equally to this work.

**Keywords:** electrolyte • Li metal battery • solid electrolyte interphase

- [1] J.-M. Tarascon, M. Armand, *Nature* **2001**, *414*, 359.
- [2] J. B. Goodenough, K.-S. Park, *J. Am. Chem. Soc.* **2013**, *135*, 1167.
- [3] M. Li, J. Lu, Z. Chen, K. Amine, *Adv. Mater.* **2018**, *30*, 1800561.
- [4] T. Kim, W. Song, D.-Y. Son, L. K. Ono, Y. Qi, *J. Mater. Chem. A* **2019**, *7*, 2942.
- [5] X. Shen, H. Liu, X.-B. Cheng, C. Yan, J.-Q. Huang, *Energy Storage Mater.* **2018**, *12*, 161.
- [6] B. V. Ratnakumar, M. C. Smart, A. Kindler, H. Frank, R. Ewell, S. Surampudi, *J. Power Sources* **2003**, *119–121*, 906.
- [7] D. Lin, Y. Liu, Y. Cui, *Nat. Nanotechnol.* **2017**, *12*, 194.
- [8] B. Liu, J.-G. Zhang, W. Xu, *Joule* **2018**, *2*, 833.
- [9] Z. A. Ghazi, Z. Sun, C. Sun, F. Qi, B. An, F. Li, H.-M. Cheng, *Small* **2019**, *15*, 1900687.
- [10] P. G. Bruce, S. A. Freunberger, L. J. Hardwick, J.-M. Tarascon, *Nat. Mater.* **2012**, *11*, 19.
- [11] J. B. Goodenough, Y. Kim, *Chem. Mater.* **2010**, *22*, 587.
- [12] K. Xu, *Chem. Rev.* **2004**, *104*, 4303.
- [13] K. Xu, *Chem. Rev.* **2014**, *114*, 11503.
- [14] Q. Wang, P. Ping, X. Zhao, G. Chu, J. Sun, C. Chen, *J. Power Sources* **2012**, *208*, 210.
- [15] B. Li, Y. Chao, M. Li, Y. Xiao, R. Li, K. Yang, X. Cui, G. Xu, L. Li, C. Yang, Y. Yu, D. P. Wilkinson, J. Zhang, *Electrochem. Energy Rev.* **2023**, *6*, 7.
- [16] U. H. Lee, K. Nam, S. H. Noh, D. Kim, J. Kang, *Adv. Sustain. Syst.* **2025**, *9*, e00413.
- [17] J. Qian, W. A. Henderson, W. Xu, P. Bhattacharya, M. Engelhard, O. Borodin, J.-G. Zhang, *Nat. Commun.* **2015**, *6*, 6362.
- [18] X. Han, Y. Gong, K. Fu, X. He, G. T. Hitz, J. Dai, A. Pearse, B. Liu, H. Wang, G. Rubloff, Y. Mo, V. Thangadurai, E. D. Wachsman, L. Hu, *Nat. Mater.* **2017**, *16*, 572.
- [19] X.-B. Cheng, R. Zhang, C.-Z. Zhao, F. Wei, J.-G. Zhang, Q. Zhang, *Adv. Sci.* **2016**, *3*, 1500213.
- [20] H. Wang, Z. Yu, X. Kong, S. C. Kim, D. T. Boyle, J. Qin, Z. Bao, Y. Cui, *Joule* **2022**, *6*, 588.
- [21] E. M. Erickson, E. Markevich, G. Salitra, D. Sharon, D. Hirshberg, E. de la Llave, I. Shterenberg, A. Rosenman, A. Frimer, D. Aurbach, *J. Electrochem. Soc.* **2015**, *162*, A2424.
- [22] X. Fan, L. Chen, X. Ji, T. Deng, S. Hou, J. Chen, J. Zheng, F. Wang, J. Jiang, K. Xu, C. Wang, *Chem* **2018**, *4*, 174.
- [23] L. Suo, W. Xue, M. Gobet, S. G. Greenbaum, C. Wang, Y. Chen, W. Yang, Y. Li, J. Li, *Proc. Natl. Acad. Sci.* **2018**, *115*, 1156.
- [24] S. Chen, J. Zheng, D. Mei, K. S. Han, M. H. Engelhard, W. Zhao, W. Xu, J. Liu, J. Zhang, *Adv. Mater.* **2018**, *30*, 1706102.
- [25] X. Ren, L. Zou, X. Cao, M. H. Engelhard, W. Liu, S. D. Burton, H. Lee, C. Niu, B. E. Matthews, Z. Zhu, C. Wang, B. W. Arey, J. Xiao, J. Liu, J.-G. Zhang, W. Xu, *Joule* **2019**, *3*, 1662.
- [26] C. Zhu, C. Sun, R. Li, S. Weng, L. Fan, X. Wang, L. Chen, M. Noked, X. Fan, *ACS Energy Lett.* **2022**, *7*, 1338.
- [27] Z. Cui, Z. Jia, D. Ruan, Q. Nian, J. Fan, S. Chen, Z. He, D. Wang, J. Jiang, J. Ma, X. Ou, S. Jiao, Q. Wang, X. Ren, *Nat. Commun.* **2024**, *15*, 2033.
- [28] L. Liu, Z. Shadike, X. Cai, M. Hong, Y. Gao, S. Shen, J. Zhang, *J. Mater. Chem. A* **2024**, *12*, 6947.
- [29] C. M. Efaw, Q. Wu, N. Gao, Y. Zhang, H. Zhu, K. Gering, M. F. Hurley, H. Xiong, E. Hu, X. Cao, W. Xu, J.-G. Zhang, E. J. Dufek, J. Xiao, X.-Q. Yang, J. Liu, Y. Qi, B. Li, *Nat. Mater.* **2023**, *22*, 1531.
- [30] Z. Li, Y. Chen, X. Yun, P. Gao, C. Zheng, P. Xiao, *Adv. Funct. Mater.* **2023**, *33*, 2300502.
- [31] Z. Yu, H. Wang, X. Kong, W. Huang, Y. Tsao, D. G. Mackanic, K. Wang, X. Wang, W. Huang, S. Choudhury, Y. Zheng, C. V. Amanchukwu, S. T. Hung, Y. Ma, E. G. Lomeli, J. Qin, Y. Cui, Z. Bao, *Nat. Energy* **2020**, *5*, 526.
- [32] H. Wang, Z. Yu, X. Kong, W. Huang, Z. Zhang, D. G. Mackanic, X. Huang, J. Qin, Z. Bao, Y. Cui, *Adv. Mater.* **2021**, *33*, 2008619.
- [33] I. R. Choi, Y. Chen, A. Shah, J. Florian, C. Serrao, J. Holoubek, H. Lyu, E. Zhang, J. H. Lee, Y. Lin, S. C. Kim, H. Park, P. Zhang, J. Lee, J. Qin, Y. Cui, Z. Bao, *Nat. Energy* **2025**, *10*, 365.
- [34] G. Zhang, T. Zhang, Z. Zhang, R. He, Q. Wang, S.-S. Chi, Y. Cui, M. D. Gu, Z. Liu, J. Chang, C. Wang, K. Xu, Y. Deng, *Nat. Commun.* **2025**, *16*, 4722.
- [35] E. Yoon, J. Lee, S. Byun, D. Kim, T. Yoon, *Adv. Funct. Mater.* **2022**, *32*, 2200026.
- [36] Z. Piao, R. Gao, Y. Liu, G. Zhou, H.-M. Cheng, *Adv. Mater.* **2023**, *35*, 2206009.
- [37] K. Matsumoto, K. Inoue, K. Nakahara, R. Yuge, T. Noguchi, K. Utsugi, *J. Power Sources* **2013**, *231*, 234.
- [38] G. Chen, L. Qiao, G. Xu, L. Li, J. Li, L. Li, X. Liu, Z. Cui, S. Zhang, S. Cheng, C. Han, S. Wang, X. Zhou, G. Cui, *Angew. Chem. Int. Ed.* **2024**, *63*, e202400797.
- [39] J. He, S. Qi, H. Wang, J. Ma, N. Artrith, *ACS Appl. Energy Mater.* **2025**, *8*, 343.
- [40] Y. Liu, D. Lin, Y. Li, G. Chen, A. Pei, O. Nix, Y. Li, Y. Cui, *Nat. Commun.* **2018**, *9*, 3656.
- [41] S. Li, W. Zhang, Q. Wu, L. Fan, X. Wang, X. Wang, Z. Shen, Y. He, Y. Lu, *Angew. Chem. Int. Ed.* **2020**, *59*, 14935.
- [42] K. Liu, W. Zhang, Q. Feng, Y. Lu, H. Wang, G. Cheng, H. Liu, Q. Cao, Z. Luo, P. Zhou, Y. Xia, W. Hou, K. Zhao, C. Du, *Nat. Commun.* **2024**, *16*, 3344.
- [43] K. Ryu, K. Lee, J. Lim, M. J. Lee, K.-H. Kim, U. H. Lee, B. L. D. Rinkel, K. Kim, S. Kim, D. Kim, D. Shin, B. McCloskey, J. Kang, S. W. Lee, *Energy Environ. Sci.* **2024**, *17*, 7772.
- [44] L. Zhang, D. Dong, A. Cresce, Q. Wei, D. Bedrov, K. Xu, T. L. Liu, *Energy Storage Mater.* **2024**, *69*, 103397.
- [45] J. H. Sung, U. H. Lee, J. Lee, B. Yu, M. I. Maulana, S. Hong, H. D. Yoo, J. Kang, J. Yu, *Adv. Energy Mater.* **2025**, 2500279.
- [46] B. Michalak, H. Sommer, D. Mannes, A. Kaestner, T. Brezesinski, J. Janek, *Sci. Rep.* **2015**, *5*, 15627.
- [47] J.-N. Zhang, Q. Li, Y. Wang, J. Zheng, X. Yu, H. Li, *Energy Storage Mater.* **2018**, *14*, 1.
- [48] C. Monroe, J. Newman, *J. Electrochem. Soc.* **2005**, *152*, A396.
- [49] Z. Zhao, W. Chen, S. Impeng, M. Li, R. Wang, Y. Liu, L. Zhang, L. Dong, J. Unruangsri, C. Peng, C. Wang, S. Namuangruk, S.-Y. Lee, Y. Wang, H. Lu, J. Guo, *J. Mater. Chem. A* **2020**, *8*, 3459.
- [50] D. Devaux, D. Glé, T. N. T. Phan, D. Gigmes, E. Giroud, M. Deschamps, R. Denoyel, R. Bouchet, *Chem. Mater.* **2015**, *27*, 4682.
- [51] R. Bouchet, S. Maria, R. Meziane, A. Aboulaich, L. Lienafa, J.-P. Bonnet, T. N. T. Phan, D. Bertin, D. Gigmes, D. Devaux, R. Denoyel, M. Armand, *Nat. Mater.* **2013**, *12*, 452.
- [52] C. Cao, Y. Li, Y. Feng, C. Peng, Z. Li, W. Feng, *Energy Storage Mater.* **2019**, *19*, 401.
- [53] S. Han, P. Wen, H. Wang, Y. Zhou, Y. Gu, L. Zhang, Y. Shao-Horn, X. Lin, M. Chen, *Nat. Mater.* **2023**, *22*, 1515.
- [54] T. Dong, J. Zhang, G. Xu, J. Chai, H. Du, L. Wang, H. Wen, X. Zang, A. Du, Q. Jia, X. Zhou, G. Cui, *Energy Environ. Sci.* **2018**, *11*, 1197.
- [55] S. Choudhury, S. Stalin, D. Vu, A. Warren, Y. Deng, P. Biswal, L. A. Archer, *Nat. Commun.* **2019**, *10*, 4398.
- [56] L. Porcarelli, C. Gerbaldi, F. Bella, J. R. Nair, *Sci. Rep.* **2016**, *6*, 19892.
- [57] J. Jie, Y. Liu, L. Cong, B. Zhang, W. Lu, X. Zhang, J. Liu, H. Xie, L. Sun, J. *Energy Chem.* **2020**, *49*, 80.
- [58] S.-Y. Zhang, Q. Zhuang, M. Zhang, H. Wang, Z. Gao, J.-K. Sun, J. Yuan, *Chem. Soc. Rev.* **2020**, *49*, 1726.
- [59] X. Wang, F. Chen, G. M. A. Girard, H. Zhu, D. R. MacFarlane, D. Mecerreyes, M. Armand, P. C. Howlett, M. Forsyth, *Joule* **2019**, *3*, 2687.
- [60] H. Wang, J. Song, K. Zhang, Q. Fang, Y. Zuo, T. Yang, Y. Yang, C. Gao, X. Wang, Q. Pang, D. Xia, *Energy Environ. Sci.* **2022**, *15*, 5149.
- [61] W. Zhang, V. Koverga, S. Liu, J. Zhou, J. Wang, P. Bai, S. Tan, N. K. Dandu, Z. Wang, F. Chen, J. Xia, H. Wan, X. Zhang, H. Yang, B. L. Lucht, A.-M. Li, X.-Q. Yang, E. Hu, S. R. Raghavan, A. T. Ngo, C. Wang, *Nat. Energy* **2024**, *9*, 386.
- [62] F. Han, A. S. Westover, J. Yue, X. Fan, F. Wang, M. Chi, D. N. Leonard, N. J. Dudney, H. Wang, C. Wang, *Nat. Energy* **2019**, *4*, 187.
- [63] J. Kasemchainan, S. Zekoll, D. S. Jolly, Z. Ning, G. O. Hartley, J. Marrow, P. G. Bruce, *Nat. Mater.* **2019**, *18*, 1105.
- [64] S. Ohta, T. Kobayashi, J. Seki, T. Asaoka, *J. Power Sources* **2012**, *202*, 332.
- [65] Y. Li, J. T. Han, C. A. Wang, H. Xie, J. B. Goodenough, *J. Mater. Chem* **2012**, *22*, 15357.
- [66] D. O. Shin, K. Oh, K. M. Kim, K.-Y. Park, B. Lee, Y.-G. Lee, K. Kang, *Sci. Rep.* **2015**, *5*, 18053.

- [67] C. Bernuy-Lopez, W. J. Manalastas, J. M. Lopez del Amo, A. Aguadero, F. Aguesse, J. A. Kilner, *Chem. Mater.* **2014**, *26*, 3610.
- [68] S.-K. Jung, H. Gwon, H. Kim, G. Yoon, D. Shin, J. Hong, C. Jung, J.-S. Kim, *Nat. Commun.* **2022**, *13*, 7638.
- [69] Y. Feng, L. Yang, Z. Yan, D. Zuo, Z. Zhu, L. Zeng, Y. Zhu, J. Wan, *Energy Storage Mater.* **2023**, *63*, 103053.
- [70] F. Aguesse, W. Manalastas, L. Buannic, J. M. L. del Amo, G. Singh, A. Llordés, J. Kilner, *ACS Appl. Mater. Interfaces* **2017**, *9*, 3808.
- [71] A. Sharafi, E. Kazayak, A. L. Davis, S. Yu, T. Thompson, D. J. Siegel, N. P. Dasgupta, J. Sakamoto, *Chem. Mater.* **2017**, *29*, 7961.
- [72] Q. Cheng, A. Li, N. Li, S. Li, A. Zangiabadi, T.-D. Li, W. Huang, A. C. Li, T. Jin, Q. Song, W. Xu, N. Ni, H. Zhai, M. Dontigny, K. Zaghib, X. Chuan, D. Su, K. Yan, Y. Yang, *Joule* **2019**, *3*, 1510.
- [73] Q. Liu, Q. Yu, S. Li, S. Wang, L. Zhang, B. Cai, D. Zhou, B. Li, *Energy Storage Mater.* **2020**, *25*, 613.
- [74] M. Kotobuki, K. Kanamura, Y. Sato, T. Yoshida, *J. Power Sources* **2011**, *196*, 7750.
- [75] J. Liu, T. Liu, Y. Pu, M. Guan, Z. Tang, F. Ding, Z. Xu, Y. Li, *RSC Adv.* **2017**, *7*, 46545.
- [76] A. Sakuda, A. Hayashi, M. Tatsumisago, *Sci. Rep.* **2013**, *3*, 2261.
- [77] N. Kamaya, K. Homma, Y. Yamakawa, M. Hirayama, R. Kanno, M. Yonemura, T. Kamiyama, Y. Kato, S. Hama, K. Kawamoto, A. Mitsui, *Nat. Mater.* **2011**, *10*, 682.
- [78] K. Takada, N. Ohta, L. Zhang, X. Xu, B. T. Hang, T. Ohnishi, M. Osada, T. Sasaki, *Solid State Ion.* **2012**, *225*, 594.
- [79] H. Park, S. Yu, D. J. Siegel, *ACS Energy Lett.* **2021**, *6*, 150.
- [80] A. L. Davis, R. Garcia-Mendez, K. N. Wood, E. Kazayak, K.-H. Chen, G. Teeter, J. Sakamoto, N. P. Dasgupta, *J. Mater. Chem. A* **2020**, *8*, 6291.
- [81] C. Wang, K. Adair, X. Sun, *Acc. Mater. Res.* **2022**, *3*, 21.
- [82] Y. Wu, J. Xu, P. Lu, J. Lu, L. Gan, S. Wang, R. Xiao, H. Li, L. Chen, F. Wu, *Adv. Energy Mater.* **2023**, *13*, 2301336.
- [83] C. Wang, K. R. Adair, J. Liang, X. Li, Y. Sun, X. Li, J. Wang, Q. Sun, F. Zhao, X. Lin, R. Li, H. Huang, L. Zhang, R. Yang, S. Lu, X. Sun, *Adv. Funct. Mater.* **2019**, *29*, 1900392.
- [84] F. Zhao, S. H. Alahakoon, K. Adair, S. Zhang, W. Xia, W. Li, C. Yu, R. Feng, Y. Hu, J. Liang, X. Lin, Y. Zhao, X. Yang, T.-K. Sham, H. Huang, L. Zhang, S. Zhao, S. Lu, Y. Huang, X. Sun, *Adv. Mater.* **2021**, *33*, 2006577.
- [85] Z. Wang, Y. Jiang, J. Wu, Y. Jiang, W. Ma, Y. Shi, X. Liu, B. Zhao, Y. Xu, J. Zhang, *Nano Energy* **2021**, *84*, 105906.
- [86] Y. Li, G. Wu, X. Fan, D. Li, H. Liu, X. Zhao, W. Ren, P. Lei, X. Zhao, X. Wang, G. Wang, L. Gao, C.-W. Nan, L.-Z. Fan, *Energy Storage Mater.* **2025**, *77*, 104221.
- [87] F. Zhao, J. Liang, C. Yu, Q. Sun, X. Li, K. Adair, C. Wang, Y. Zhao, S. Zhang, W. Li, S. Deng, R. Li, Y. Huang, H. Huang, L. Zhang, S. Zhao, S. Lu, X. Sun, *Adv. Energy Mater.* **2020**, *10*, 1903422.
- [88] S. Li, S.-J. Yang, G.-X. Liu, J.-K. Hu, Y.-L. Liao, X.-L. Wang, R. Wen, H. Yuan, J.-Q. Huang, Q. Zhang, *Adv. Mater.* **2024**, *36*, 2307768.
- [89] C. Wei, Z. Wu, S. Li, Z. Jiang, L. Li, X. Wang, P. Ouyang, Z. Lu, M. Deng, H. Yang, C. Yu, *Mater. Sci. Eng. R Rep.* **2025**, *164*, 100950.
- [90] H. Muramatsu, A. Hayashi, T. Ohtomo, S. Hama, M. Tatsumisago, *Solid State Ion.* **2011**, *182*, 116.
- [91] P. Lu, D. Wu, L. Chen, H. Li, F. Wu, *Electrochem. Energy Rev.* **2022**, *5*, 3.
- [92] J. Zhang, X. Gu, *Rare Met.* **2023**, *42*, 47.
- [93] Z. D. Hood, A. U. Mane, A. Sundar, S. Tepavcevic, P. Zapol, U. D. Eze, S. P. Adhikari, E. Lee, G. E. Sterbinsky, J. W. Elam, J. G. Connell, *Adv. Mater.* **2023**, *35*, 2300673.
- [94] W. D. Jung, M. Jeon, S. S. Shin, J.-S. Kim, H.-G. Jung, B.-K. Kim, J.-H. Lee, Y.-C. Chung, H. Kim, *ACS Omega* **2020**, *5*, 26015.
- [95] J. Liang, N. Chen, X. Li, X. Li, K. R. Adair, J. Li, C. Wang, C. Yu, M. N. Banis, L. Zhang, S. Zhao, S. Lu, H. Huang, R. Li, Y. Huang, X. Sun, *Chem. Mater.* **2020**, *32*, 2664.
- [96] F. Wu, W. Fitzhugh, L. Ye, J. Ning, X. Li, *Nat. Commun.* **2018**, *9*, 4037.
- [97] S.-J. Choi, S.-H. Choi, A. D. Bui, Y.-J. Lee, S.-M. Lee, H.-C. Shin, Y.-C. Ha, *ACS Appl. Mater. Interfaces* **2018**, *10*, 31404.
- [98] Z. Liu, W. Fu, E. A. Payzant, X. Yu, Z. Wu, N. J. Dudney, J. Kiggans, K. Hong, A. J. Rondinone, C. Liang, *J. Am. Chem. Soc.* **2013**, *135*, 975.
- [99] Y. Kato, S. Hori, T. Saito, K. Suzuki, M. Hirayama, A. Mitsui, M. Yonemura, H. Iba, R. Kanno, *Nat. Energy* **2016**, *1*, 16030.
- [100] H. Li, Q. Lin, J. Wang, L. Hu, F. Chen, Z. Zhang, C. Ma, *Angew. Chem. Int. Ed.* **2024**, *63*, e202407892.
- [101] W. Liu, S. W. Lee, D. Lin, F. Shi, S. Wang, A. D. Sendek, Y. Cui, *Nat. Energy* **2017**, *2*, 17035.
- [102] Y. Zhang, R. Chen, S. Wang, T. Liu, B. Xu, X. Zhang, X. Wang, Y. Shen, Y.-H. Lin, M. Li, L.-Z. Fan, L. Li, C.-W. Nan, *Energy Storage Mater.* **2020**, *25*, 145.
- [103] J. Hu, C. Lai, K. Chen, Q. Wu, Y. Gu, C. Wu, C. Li, *Nat. Commun.* **2022**, *13*, 7914.
- [104] Q. Wu, M. Fang, S. Jiao, S. Li, S. Zhang, Z. Shen, S. Mao, J. Mao, J. Zhang, Y. Tan, K. Shen, J. Lv, W. Hu, Y. He, Y. Lu, *Nat. Commun.* **2023**, *14*, 6296.
- [105] Q. Pan, D. M. Smith, H. Qi, S. Wang, C. Y. Li, *Adv. Mater.* **2015**, *27*, 5995.
- [106] S. Choudhury, in *Ration. Des. Nanostructured Polym. Electrolytes Solid-Liquid Interphases Lithium Batter.* (Ed: S. Choudhury), Springer International Publishing, Cham **2019**, pp. 35–57.
- [107] A. Li, X. Liao, H. Zhang, L. Shi, P. Wang, Q. Cheng, J. Borovilas, Z. Li, W. Huang, Z. Fu, M. Dontigny, K. Zaghib, K. Myers, X. Chuan, X. Chen, Y. Yang, *Adv. Mater.* **2020**, *32*, 1905517.
- [108] Y. Wang, J. Ju, S. Dong, Y. Yan, F. Jiang, L. Cui, Q. Wang, X. Han, G. Cui, *Adv. Funct. Mater.* **2021**, *31*, 2101523.
- [109] Z. Li, A. Li, H. Zhang, R. Lin, T. Jin, Q. Cheng, X. Xiao, W.-K. Lee, M. Ge, H. Zhang, A. Zangiabadi, I. Waluyo, A. Hunt, H. Zhai, J. J. Borovilas, P. Wang, X.-Q. Yang, X. Chuan, Y. Yang, *Nano Energy* **2020**, *72*, 104655.
- [110] Q. Guo, Y. Han, H. Wang, S. Xiong, Y. Li, S. Liu, K. Xie, *ACS Appl. Mater. Interfaces* **2017**, *9*, 41837.
- [111] L. Liu, Z. Shadike, N. Wang, Y. Chen, X. Cai, E. Hu, J. Zhang, *eScience* **2024**, *4*, 100268.
- [112] Q. Xu, T. Li, Z. Ju, G. Chen, D. Ye, G. I. N. Waterhouse, Y. Lu, X. Lai, G. Zhou, L. Guo, K. Yan, X. Tao, H. Li, Y. Qiu, *Nature* **2025**, *637*, 339.
- [113] Y. Li, S. Kumar, G. Yang, J. Lu, Y. Yao, K. Kang, Z. W. Seh, *Science* **2025**, *389*, eadl5482.
- [114] J. Kang, H. Chung, C. Doh, B. Kang, B. Han, *J. Power Sources* **2015**, *293*, 11.
- [115] Y. Zhu, X. He, Y. Mo, *ACS Appl. Mater. Interfaces* **2015**, *7*, 23685.
- [116] A. Jain, S. P. Ong, G. Hautier, W. Chen, W. D. Richards, S. Dacek, S. Cholia, D. Gunter, D. Skinner, G. Ceder, K. A. Persson, *APL Mater.* **2013**, *1*, 011002.
- [117] J. Yoon, S. Park, Y. Yang, U. H. Lee, J. Kang, *Korean J. Mater. Res.* **2025**, *35*, 18.
- [118] P. de Blasio, J. Elsborg, T. Vegge, E. Flores, A. Bhowmik, *Sci. Data* **2024**, *11*, 750.
- [119] S. C. Kim, S. T. Oyakhire, C. Athanatis, J. Wang, Z. Zhang, W. Zhang, D. T. Boyle, M. S. Kim, Z. Yu, X. Gao, T. Sogade, E. Wu, J. Qin, Z. Bao, S. F. Bent, Y. Cui, *Proc. Natl. Acad. Sci.* **2023**, *120*, e2214357120.
- [120] K. A. Severson, P. M. Attia, N. Jin, N. Perkins, B. Jiang, Z. Yang, M. H. Chen, M. Aykol, P. K. Herring, D. Fragedakis, M. Z. Bazant, S. J. Harris, W. C. Chueh, R. D. Braatz, *Nat. Energy* **2019**, *4*, 383.

Manuscript received: July 19, 2025

Revised manuscript received: October 26, 2025

Version of record online: